

Simulating stochastic population dynamics: The Linear Noise Approximation can capture non-linear phenomena

Frederick Truman-Williams^a and Giorgos Minas^{b,1}

^a*Mathematical Institute, University of Oxford, Oxford, OX2 6GG, United Kingdom*

^b*School of Mathematics and Statistics, University of St Andrews, St Andrews, KY16 9SS, Scotland, United Kingdom**

Abstract

There is an abundance of highly stochastic, non-linear phenomena present in population dynamics across various fields, including molecular biology, epidemiology, and ecology. Oscillations and multi-stability are particularly prevalent in gene regulation systems. None of the currently available stochastic models for population dynamics are accurate and computationally efficient for long-term predictions. A prominent model in this field, known as the Linear Noise Approximation (LNA), is computationally efficient for tasks such as simulation, sensitivity analysis, and parameter estimation, still, it is only accurate for linear systems and short-time predictions. Other models may achieve greater accuracy across a broader range of systems, but they sacrifice computational efficiency and analytical tractability. This paper demonstrates that, with specific modifications, the LNA can indeed accurately capture non-linear dynamics in population dynamics. We introduce a new framework that employs centre manifold theory, a classical concept in non-linear dynamical systems. This approach allows us to identify simple, specialised modifications to the LNA tailored to classes of qualitatively similar non-linear dynamical systems. With these modifications, the LNA can achieve accurate long-term predictions without compromising its computational efficiency. We apply our methodology to a class of oscillatory systems and a class of bi-stable systems, and we provide multiple examples in molecular population dynamics that showcase accurate long-term predictions, and significant improvements in computational efficiency.

1 Introduction

In molecular biology, ecology, epidemiology and other fields, there is a plethora of non-linear dynamical phenomena such as oscillations and multi-stabilities. Examples include the circadian rhythms [21], embryonic development oscillations [39], cell signalling oscillations [4], multi-stabilities in cell cycle [45, 46, 2], cell differentiation [8, 19], and apoptosis [3], the central carbon metabolism in *E.coli* [26], predator-prey oscillations in ecology [11], and epidemic oscillations [62]. These non-linear dynamics are caused by feed-forward loops [38], negative feedback loops [38, 48] and other mechanisms, which are operated by networks of interacting species. For example, gene expression oscillations are often generated when a gene directly suppresses its own expression or activates the expression of its suppressors. In infectious diseases outbreaks, compartments of the population, such as infected and susceptible individuals, interact between each other and phenomena like awareness and fatigue can generate oscillatory behaviors [62]. The

*To whom correspondence should be addressed. E-mail: gm256@st-andrews.ac.uk

effects of stochasticity in these interactions between different populations, caused by molecular diffusion or, more generally, the complex environment in which these interactions occur, are significant, especially when dealing with smaller populations. Yet modeling the stochasticity using fast, accurate, scalable methods is an unsolved problem.

These networks of stochastic interactions between different populations are often called reaction networks. The term reaction is not only used for biochemical reactions but any event that directly causes a change in the population of one or more species or groups. The stochastic dynamics of reaction networks, can be described, under certain assumptions, by Markov processes $\{\mathbf{Y}(t) = (Y_1(t), \dots, Y_n(t))^T : t \geq 0\}$, describing the evolution of n different populations over time. The so-called (chemical) master equation [13], which describes the evolution of the probability distribution of the species populations, can be solved only rarely, severely limiting its tractability. The stochastic simulation algorithm (SSA) [14] produces exact simulations of the master equation but it is far too slow to be used in most applied settings since it simulates every single reaction event.

At present, there are several methods available for approximating the master equation, which aim to accelerate simulations. Notable examples include tau leaping algorithms [17, 18] and the numerical integration of the (chemical) Langevin equations [16]. Both of these approaches significantly increase simulation speed; however, they leave no scope for the analytical study of the probability distributions of the populations and can be extremely slow for sensitivity analysis and parameter estimation. Other recent methods [6, 28] focus on simplifying protein-binding reactions, which frequently appear in molecular biology networks.

Much work has followed from van Kampen's system size expansion [58], which uses a system size parameter Ω (like cell volume in molecular biology, maximum population size in ecology or epidemiology) to derive approximations of the master equation. Under certain conditions, the deterministic process $\{\mathbf{x}(t) : t \geq 0\}$ which solves the macroscopic reaction-rate equations was shown to be the limit, as $\Omega \rightarrow \infty$, of the solutions of the master equation [32, 33]. The Linear Noise Approximation (LNA), derived using the system size expansion, is a stochastic model that provides even more rapid simulation than the aforementioned stochastic methods as well as being the only model in this field that allows analytical expressions of probability distributions of populations at arbitrary time-points. This makes the LNA a powerful tool for sensitivity analysis and statistical inference [41, 42, 54, 43, 31, 10, 20, 49].

However, the important drawback of using the LNA is its inability to approximate the long-term behavior of non-linear population dynamics. Indeed, when the system dynamics are non-linear [61], predictions of the state of the system at time t given the state at an earlier time s become inaccurate as $t - s$ becomes large. For a given system, we can qualitatively examine the dynamics of its paths and identify different phases in the populations' evolution - for instance their peaks and troughs. If we were to examine the distribution of entire stochastic paths generated by the SSA in a finite number of time-points then we find that, the phases of such paths become out of sync with what the LNA predicts their phases to be. Hence the LNA makes incorrect predictions of the dynamics thereafter. In [41], it was shown that in the specific setting where the macroscopic ($\Omega \rightarrow \infty$) deterministic approximation has an attractive limit cycle solution, correcting these drifts in phase predicted by the LNA is sufficient to produce simulations that are nearly identical to those produced by the SSA. This approach enables the construction of both fast and accurate algorithms for stochastic simulation, sensitivity analysis, and statistical inference of this class of non-linear systems [41].

There are three main results in this paper. Firstly, we show that the analytically tractable LNA model, which is known to be long-time accurate only for linear systems, can also be applied to non-linear systems after appropriate modifications. In particular, we illustrate that it *can* accurately describe long-term stochastic dynamics for arguably the two most abundant non-linear phenomena: oscillations and bi-stability. We demonstrate this on several systems including

the oscillatory systems in [35, 63, 4], and bi-stable systems in [12, 2, 19]. Secondly, as part of this effort, we develop a novel framework for constructing LNA-based models for non-linear dynamical systems. We adopt the term phase-corrected LNA (pcLNA)—originally introduced in [41]—to describe this stochastic modelling approach, which evolves the system using LNA equations while periodically adjusting the phase to mitigate phase drift. Fundamental to the pcLNA approach is a mapping G that computes the phase of any stochastic state allowing for any phase drift to be corrected. We show that for the very large class of systems whose macroscopic reaction rate equation exhibits a non-hyperbolic equilibrium, the theory of centre manifolds of dynamical systems can be employed to explicitly define the phase correction map G . Thirdly, we illustrate *how* the pcLNA framework can be applied to accurately describe reaction networks whose macroscopic deterministic evolution $\{\mathbf{x}(t) : t \geq 0\}$ exhibits Hopf bifurcation and those exhibiting bi-stability in a region of their parameter space (see Figure 1). That is, systems with oscillations; sustained or non-sustained and often determined by only a small change in a parameter, or systems which can switch between two steady states due to stochasticity. We demonstrate that the pcLNA model for these systems offers accurate approximations of the master equation for long-term simulation whilst substantially reducing the simulation time by several orders of magnitude. A key implication of this accuracy is that it enables the tractability of pcLNA models to be harnessed for computationally intensive tasks such as sensitivity analysis, inference, and prediction.

While the approach developed in [41] demonstrated that phase correction significantly improves the long-term accuracy of the LNA in oscillatory systems with stable limit cycles, it was limited to this specific dynamics. In contrast, the framework introduced in this paper generalises the concept of phase correction by introducing centre manifold theory to define and correct phase drifts to a broad class of systems only assumed to have a non-hyperbolic equilibrium, which includes the abundant classes of oscillatory and bi-stable systems. This theoretical foundation enables us to construct a unified, algorithmic approach for defining and correcting phase across diverse nonlinear regimes, allowing the pcLNA to extend the analytical tractability and computational efficiency of the LNA to a class of systems found in a wide range of scientific subjects.

We begin in Section 2 by introducing the pcLNA modelling framework. We first review reaction networks and the system size expansion in Sections 2.1 and 2.2, before introducing the Linear Noise Approximation (LNA) in Section 2.3. We then discuss the LNA’s loss of accuracy in non-linear systems and introduce the concept of phase in this context. In Section 2.4, we present the general phase corrected LNA (pcLNA), followed by a discussion on how to define the phase correction map—using centre manifold theory—in Section 2.5. In Section 3, we apply our framework to reaction networks whose macroscopic reaction rate equation undergoes a Hopf bifurcation and develop the pcLNA algorithm specific to these systems. Section 4 focuses on bi-stable systems and constructs the corresponding pcLNA algorithms. We validate our framework through numerical investigations in Section 5, and conclude with a discussion of our findings and future directions in Section 6. Additional numerical investigations demonstrating the accuracy of the pcLNA modelling techniques on other reaction networks, as well as supporting technical results and derivations, are provided in the Supporting Information (SI).

2 The pcLNA modelling framework

2.1 Population dynamics

We begin by presenting a mathematical formulation of population dynamics evolving through reaction networks. We describe this framework within the context of molecular biology, although

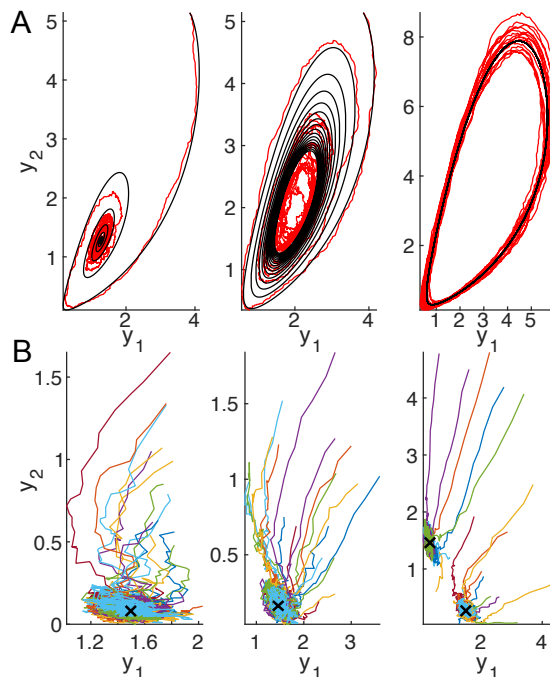
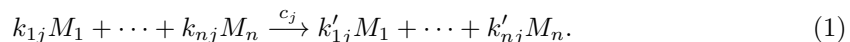


Figure 1: A. Phase portraits of solutions of the RRE in (6) (black) and a SSA simulation (red) for the system in [63]. B. Phase portraits of 20 SSA simulations (color) and the equilibria of the RRE in (6) (crosses) for the system in [12]. The qualitative changes from left to right figure are due to changes in the bifurcation parameter value.

analogous terminology can be applied in other fields such as epidemiology and ecology (see, for instance, [20, 64] and Figure 2).

A system of multiple different molecular sub-populations, M_1, M_2, \dots, M_n has state vector, $\mathbf{Y}(t) = (Y_1(t), \dots, Y_n(t))^T$ where $Y_i(t) \geq 0$, $i \in \{1, \dots, n\}$, denotes the number of M_i molecules at time t . These molecules undergo reactions R_j , $j \in \{1, \dots, r\}$, such as transcription, translation, degradation and translocation, which change the number of molecules of each specie,



Here, the non-negative coefficients $k_{ij}, k'_{ij} \geq 0$ denote the number of molecules of M_i involved as reactants and products, respectively, in reaction R_j . If R_j occurs at time $t \geq 0$, $\mathbf{Y}(t)$ jumps to a new state $\mathbf{Y}(t) + \boldsymbol{\nu}_j$, where the transition vectors $\boldsymbol{\nu}_j = (k'_{1j} - k_{1j}, \dots, k'_{nj} - k_{nj})^T \in \mathbb{R}^n$ are often called stoichiometric. Under the assumption that these reactions occur in a well-mixed solution [14], we can derive the propensity functions $\pi_j : \mathbb{R}^n \rightarrow [0, \infty)$ for each $j \in \{1, \dots, r\}$ with the probability of one R_j reaction occurring in the next infinitesimal time interval $[t, t + dt)$

$$P(\mathbf{Y}(t + dt) - \mathbf{Y}(t) = \boldsymbol{\nu}_j) = \pi_j(\mathbf{Y}(t))dt + o(dt^2). \quad (2)$$

The propensity functions π_j along with the stoichiometric vector $\boldsymbol{\nu}_j$, $j = 1, \dots, r$ completely specify the evolution of the reaction network.

The general form of the propensity function of the reaction in (1) is $\pi_j(\mathbf{y}) = c_j \prod_i y_i^{k_{ij}}$, with uni-molecular ($M_i \xrightarrow{c_j} \cdot$) and bi-molecular reactions ($M_i + M_{i'} \xrightarrow{c_j} \cdot$) with propensity of the form $c_j y_i$ and $c_j y_i y_{i'}$, respectively, being the most common type [60]. Here $c_j \in \mathbb{R}$ is the reaction

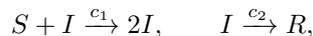
rate constant corresponding to reaction R_j . The propensity functions are not restricted to the above general form. For instance, for enzymatic reactions involving species M_i the propensity has the Michaelis-Menten form [29], $c_2 y_i / (c_1 + y_i)$, while the Hill form [24], $c_2 y_i^h / (c_1^h + y_i^h)$, is also often used to reflect cooperative binding. For a discussion on the latter forms of propensities see [6].

These conditions give rise to a time-inhomogeneous, discrete state-space Markov process $\{\mathbf{Y}(t) : t \geq 0\}$. The Kolmogorov forward equation [15] describing the evolution of the probability distribution, $P(\mathbf{y}, t) := P(\mathbf{Y}(t) = \mathbf{y} \mid \mathbf{Y}(0) = \mathbf{y}_0)$, of the stochastic process $\{\mathbf{Y}(t) : t \geq 0\}$ is,

$$\frac{\partial P(\mathbf{y}, t)}{\partial t} = \sum_{j=1}^r \pi_j(\mathbf{y} - \boldsymbol{\nu}_j) P(\mathbf{y} - \boldsymbol{\nu}_j, t) - \sum_{j=1}^r \pi_j(\mathbf{y}) P(\mathbf{y}, t). \quad (3)$$

The Kolmogorov equation is often referred as (chemical) master equation. Despite the equation only being analytically tractable for few cases, an exact simulation algorithm is available, namely Gillespie's stochastic simulation algorithm (SSA) [14]. We provide details of this in SI (Section S1).

Example (SIR model): The SIR model used to describe population dynamics in infectious disease outbreaks is an example of a reaction network. We formulate it here to provide a concrete example of our general formulation above (see also Figure 2(A-B) for a summary). In the SIR network, there are three populations, say M_1, M_2, M_3 , corresponding to the Susceptible (S), Infected (I), and Recovered (R) individuals. Two reactions, that is infection and recovery, say R_1 and R_2 , can take place and can be described by



where here c_1 and c_2 are the reaction rate constants for the two reactions. The state vector $\mathbf{Y} = (Y_1, Y_2, Y_3)$ corresponds to the three populations M_1 (S), M_2 (I), and M_3 (R). The propensity functions are

$$\pi_1(\mathbf{Y}) = c_1 Y_1 Y_2, \quad \pi_2(\mathbf{Y}) = c_2 Y_2$$

and the corresponding stoichiometry vectors $\mathbf{v}_1 = (-1, +1, 0)$ and $\mathbf{v}_2 = (0, -1, +1)$. This can be used to formulate Equation (3) for this system.

2.2 System Size Expansion

The time-evolution of the stochastic process $\{\mathbf{Y}(t) : t \geq 0\}$ can be described using the random time change representation (RTC) [1]

$$\mathbf{Y}(t) = \mathbf{Y}(0) + \sum_{j=1}^r \boldsymbol{\nu}_j N_j \left(\int_0^t \pi_j(\mathbf{Y}(s)) ds \right), \quad (4)$$

where, for $j \in \{1, \dots, r\}$, N_j are independent, unit Poisson processes corresponding to reaction R_j . This implies that for a given trajectory $\mathbf{Y}(s)$, $s \in [0, t]$, the random variables $N_j \left(\int_0^t \pi_j(\mathbf{Y}(s)) ds \right)$ are independent and have Poisson distribution with mean $\int_0^t \pi_j(\mathbf{Y}(s)) ds$.

In pursuit of seeking methods to approximate the process $\{\mathbf{Y}(t) : t \geq 0\}$, it is common to introduce a system size parameter Ω . Through setting $\mathbf{X}(t) := \mathbf{Y}(t)/\Omega$, one can study the dependence of stochastic fluctuations upon system size. It is sufficient to assume that the rates $\pi_j(\mathbf{Y}(t))$ depend upon Ω as $\pi_j(\mathbf{Y}(t)) := \Omega \rho_j(\mathbf{Y}(t)/\Omega)$ where ρ_j are called macroscopic rates

of the system. This is a fairly-relaxed condition, that can be further relaxed to more general relations between the two functions [58, 33].

Using this condition, we can re-write the infinitesimal RTC equation in (4) in terms of $\mathbf{X}(t)$ as

$$\mathbf{X}(t + dt) - \mathbf{X}(t) = \sum_{j=1}^r \boldsymbol{\nu}_j N_j (\Omega \rho_j(\mathbf{X}(t)) dt) / \Omega, \quad (5)$$

with $\mathbf{X}(0) = \mathbf{X}_0$, thus providing a time evolution law for the process $\{\mathbf{X}(t) : t \geq 0\}$. If, for each $t \geq 0$, we define $\mathbf{x}(t)$ as the limit in probability of $\mathbf{X}(t)$ as $\Omega \rightarrow \infty$, we can use the law of large numbers¹ (see [32, 33]) to derive the limit of equation (5), as $\Omega \rightarrow \infty$,

$$\mathbf{x}(t + dt) - \mathbf{x}(t) = \sum_{j=1}^r \boldsymbol{\nu}_j \rho_j(\mathbf{x}(t)) dt, \quad \mathbf{x}(0) = \mathbf{x}_0.$$

Letting $dt \rightarrow 0$ we derive the macroscopic reaction rate equation (RRE), corresponding to the classical mass-action kinetics. Typical in applied biochemical settings is the need to study the qualitative changes in the dynamics of $\{\mathbf{X}(t) : t \geq 0\}$ and $\{\mathbf{x}(t) : t \geq 0\}$ when one (or more) of the system parameters, say α , is free to vary. To emphasize this dependence on parameter $\alpha \in \mathbb{R}$ we write the RRE as

$$\dot{\mathbf{x}} = \frac{d\mathbf{x}}{dt} = \mathbf{F}(\mathbf{x}, \alpha), \quad \mathbf{F}(\mathbf{x}, \alpha) = \sum_{j=1}^r \boldsymbol{\nu}_j \rho_j(\mathbf{x}(t), \alpha), \quad \mathbf{x}(0) = \mathbf{x}_0. \quad (6)$$

and the corresponding Jacobian matrix

$$\mathbf{J} = \mathbf{J}(\mathbf{x}, \alpha) = (\partial F_i / \partial x_j)_{i,j=1}^n. \quad (7)$$

We will refer to the parameter α as the bifurcation parameter.

Example (SIR model, continued): If we define a system size parameter Ω (e.g. total population) for the SIR model above, then we can apply system size expansion. The reaction rates are set to satisfy $\pi_j(\mathbf{Y}(t)) := \Omega \rho_j(\mathbf{Y}(t)/\Omega)$, and hence for $\mathbf{x} = \mathbf{Y}/\Omega$ we get

$$\begin{aligned} \pi_1(\mathbf{Y}) &= c_1 Y_1 Y_2 = \Omega \tilde{c}_1 x_1 x_2 = \Omega \rho_1(\mathbf{x}), & \rho_1(\mathbf{x}) &= \tilde{c}_1 x_1 x_2, & \tilde{c}_1 &= \Omega c_1 \\ \pi_2(\mathbf{Y}) &= c_2 Y_2 = \Omega c_2 x_2 = \Omega \rho_2(\mathbf{x}), & \rho_2(\mathbf{x}) &= c_2 x_2 \end{aligned}$$

which together with the stoichiometry vectors give the RRE

$$\begin{aligned} \dot{x}_1 &= dx_1/dt = -\tilde{c}_1 x_1 x_2 \\ \dot{x}_2 &= dx_2/dt = +\tilde{c}_1 x_1 x_2 - c_2 x_2 \\ \dot{x}_3 &= dx_3/dt = +c_2 x_2. \end{aligned}$$

2.3 The Linear Noise Approximation (LNA)

To take into account the stochasticity of interactions between (molecular or other) populations, one approach is to define the LNA ansatz equation [58, 32, 33] that describes the relation between the stochastic process $\{\mathbf{X}(t) : t \geq 0\}$ and a deterministic solution $\gamma = \{\mathbf{x}(t) : t \geq 0\}$ of the RRE

¹Note that for a sequence X_1, X_2, \dots , of independent $\text{Poi}(\lambda)$ random variables ($0 < \lambda < \infty$), $N^{-1} \sum_{i=1}^N X_i$ converges in probability to λ , as $N \rightarrow \infty$.

system in (6). Their difference, scaled by $\Omega^{-1/2}$, is a stochastic process, $\{\boldsymbol{\xi}(t) : t \geq 0\}$, with $\boldsymbol{\xi}(t)$ quantifying the noisy deviations away from $\mathbf{x}(t)$. That is, for each $t \geq 0$,

$$\mathbf{X}(t) = \mathbf{x}(t) + \Omega^{-1/2} \boldsymbol{\xi}(t). \quad (8)$$

As we show in SI (Section S2) by applying a derivation similar to [1] we get that for sufficiently large values of Ω , the time-evolution of $\{\boldsymbol{\xi}(t), t \geq 0\}$ can be described by the linear Stochastic Differential equation (in the Itô sense)

$$d\boldsymbol{\xi} = \mathbf{J}_t \boldsymbol{\xi} dt + \mathbf{E}_t d\mathbf{B}_t, \quad (9)$$

where $\mathbf{J}_t = \mathbf{J}(\mathbf{x}(t))$ is the Jacobian matrix in (7) evaluated at $\mathbf{x}(t)$, \mathbf{B}_t an n -dimensional Wiener process [64], and

$$\mathbf{E}_t = \mathbf{E}(\mathbf{x}(t)) = \mathbf{S} \text{diag} \left(\sqrt{\rho_1(\mathbf{x}(t))}, \dots, \sqrt{\rho_r(\mathbf{x}(t))} \right) \quad (10)$$

the product of the stoichiometry matrix $\mathbf{S} = [\boldsymbol{\nu}_1 \cdots \boldsymbol{\nu}_r]$, and the square root of the diagonal matrix, with main diagonal entries the reaction rates $(\rho_1(\mathbf{x}(t)), \dots, \rho_r(\mathbf{x}(t)))$.

This linear SDE in (9) has a solution that, for $0 \leq s \leq t < \infty$, can be written as

$$\boldsymbol{\xi}(t) = \mathbf{C}(s, t) \boldsymbol{\xi}(s) + \boldsymbol{\eta}(s, t), \quad \boldsymbol{\eta}(s, t) \sim \text{MVN}(0, \mathbf{D}(s, t)). \quad (11)$$

where $\mathbf{C}(s, t)$ the fundamental matrix of (6), i.e. the solution of the initial value problem

$$\dot{\mathbf{C}} = \mathbf{J}_t \mathbf{C}, \quad \mathbf{C}(s, s) = \mathbf{I}, \quad (12)$$

and $\mathbf{D}(s, t)$ the symmetric, positive-definite matrix that is a solution of the initial value problem

$$\dot{\mathbf{D}} = \mathbf{J}_t \mathbf{D} + \mathbf{D} \mathbf{J}_t^T + \mathbf{E}_t \mathbf{E}_t^T, \quad \mathbf{D}(s, s) = \mathbf{0}. \quad (13)$$

Here we write \mathbf{I} for the identity matrix and $\mathbf{0}$ for the zero matrix. We also write $\text{MVN}(\mathbf{m}, \mathbf{S})$ for the Multivariate Normal (Gaussian) distribution with mean \mathbf{m} , and variance matrix \mathbf{S} .

The above representation implies that by solving the initial value problems in (6), (12) and (13), and starting with an initial condition for $\boldsymbol{\xi}(0) = \boldsymbol{\xi}_0$ drawn from an arbitrary MVN distribution, one can easily derive the MVN probability distribution of $\boldsymbol{\xi}(t)$, for any time $t > 0$. In this case, we say the LNA prediction for $\mathbf{X}(t)$ was initialised at time $s = 0$. The process $\{\mathbf{X}(t) : t \geq 0\}$ modeled by the LNA is only an approximation of the true dynamics of the reaction network $\{\mathbf{Y}(t)/\Omega : t \geq 0\}$ where $\{\mathbf{Y}(t) : t \geq 0\}$ evolves according to (4) by the SSA. Therefore, when we refer to the notion of accuracy, we mean the accuracy in the distribution of $\mathbf{X}(t)$ when trying to capture the distribution of $\mathbf{Y}(t)/\Omega$ for each $t \geq 0$, where $\{\mathbf{Y}(t) : t \geq 0\}$ evolves according to (4).

Example (SIR model, continued): To apply the LNA to the SIR reaction network, we first need to compute the Jacobian matrix by differentiation, which gives

$$\mathbf{J} = \begin{pmatrix} -\tilde{c}_1 x_2 & -\tilde{c}_1 x_1 & 0 \\ \tilde{c}_1 x_2 & \tilde{c}_1 x_1 - c_2 & 0 \\ 0 & c_2 & 0 \end{pmatrix}$$

and the matrix defined in (10), which is

$$\mathbf{E} = \begin{pmatrix} -1 & 0 \\ +1 & -1 \\ 0 & +1 \end{pmatrix} \begin{pmatrix} \sqrt{\tilde{c}_1 x_1 x_2} & 0 \\ 0 & \sqrt{c_2 x_2} \end{pmatrix} = \begin{pmatrix} -\sqrt{\tilde{c}_1 x_1 x_2} & 0 \\ \sqrt{\tilde{c}_1 x_1 x_2} & -\sqrt{c_2 x_2} \\ 0 & \sqrt{c_2 x_2} \end{pmatrix}.$$

These matrices depend on the solution, $\{\mathbf{x}(t) = (x_1(t), x_2(t), x_3(t)) : t \geq 0\}$, of the RRE in (6). Solving (12) and (13) using the above matrices gives the matrices $\mathbf{C}(s, t)$ and $\mathbf{V}(s, t)$ required to derive the distribution of $\boldsymbol{\xi}(t)$ in (11) and in turn the state $\mathbf{X}(t)$ in (8).

2.3.1 Accuracy of the LNA

The LNA accurately approximates the master equation in specific contexts. As discussed in SI (Section S2), the LNA is derived using the Central Limit Theorem, as Ω tends to ∞ , as an approximation of the probability distribution function satisfying the master equation. As a result, we expect the LNA to be accurate when Ω is sufficiently large. The value of Ω needed to ensure accuracy depends on the characteristics of the system’s dynamics and the length of time interval where the approximation is sought.

For any given finite Ω , if the LNA accurately represents the distribution of the state of a given system at some time-point, it is expected to maintain this accuracy for a subsequent short time interval. The duration for which the LNA remains accurate is influenced by the dynamics of the system and the level of stochasticity present. For instance, it was observed in [41] that for periodic systems with a moderate size Ω , the time interval over which the LNA retains its accuracy is approximately equal to the period of the system.

In situations where the system displays linear dynamics (i.e. the propensity functions in (2) are linear with respect to $\mathbf{Y}(t)$) the first two moments of the LNA coincide with those of solutions of the master equation [36]. Additionally, empirical studies comparing the distribution of the system at specific time-points, as predicted by the LNA, with histograms of the state distribution derived by simulated trajectories using the SSA, have shown agreement when the initial conditions are in the vicinity of stable equilibrium points (see for instance, [56, 41, 50], and Figure 2(B)). Recent results identified the precise generic conditions under which the LNA is accurate near equilibrium points [22].

It is important to note that, for moderate system sizes, the LNA tends to fail in approximating the long-term dynamics of multi-stable and oscillatory systems (see [50, 5, 27, 56, 41] and Figure 2(C-D)).

2.3.2 Phase

Important in diagnosing this issue, and indeed the rest of this paper, is the idea of phase. For a given reaction network, we can qualitatively examine the dynamics of its paths and identify different stages of their evolution. For example, a phase could correspond to a specific species’ peak or trough or intermediate point in the evolution of an oscillatory system or a point leading to one of the equilibria of a multi-stable system. For a stochastic path $\{\mathbf{X}(t) : t \geq 0\}$ and its deterministic path $\{\mathbf{x}(t) : t \geq 0\}$ we are able to isolate the points $\mathbf{X}(s)$ and $\mathbf{x}(s)$ at any time $s \geq 0$ on their path and qualitatively say what stages $\mathbf{X}(s)$ and $\mathbf{x}(s)$ are in with respect to the evolution of the entire path. We call these stages the phase of $\mathbf{X}(s)$ and $\mathbf{x}(s)$ respectively. Note that due to stochasticity, the phase of $\mathbf{X}(s)$ and the phase of $\mathbf{x}(s)$ can be different, particularly for large s .

We also note that the consideration of phase is only useful for non-linear systems, since for linear systems, all trajectories lead to the same nearby equilibrium as $t \rightarrow \infty$ (or $t \rightarrow -\infty$). For networks with non-linear dynamics (e.g. oscillatory or multi-stable), once the LNA becomes inaccurate at some time-point τ , the phase of $\mathbf{X}(s)$, for $s \geq \tau$, becomes out of sync with the phase of $\mathbf{x}(s)$ causing $\xi(s)$ to be too large for the LNA to make accurate predictions, even for short time transitions. That is, for times $s \geq \tau$, there will be no agreement between the LNA and SSA paths, at least for the next time interval. We call this phenomenon a phase drift.

Therefore, initialising the LNA to the correct phase is a necessary condition for the LNA to be accurate. This leads us to speculate, if one can continually initialise the LNA with the correct phase so that the phase of the stochastic and deterministic trajectory are in agreement, and $\xi(s)$ remains sufficiently small for all $s \geq 0$, then the LNA will remain accurate at all times and produce paths agreeing to those from the SSA. We argue that, for some classes of dynamical

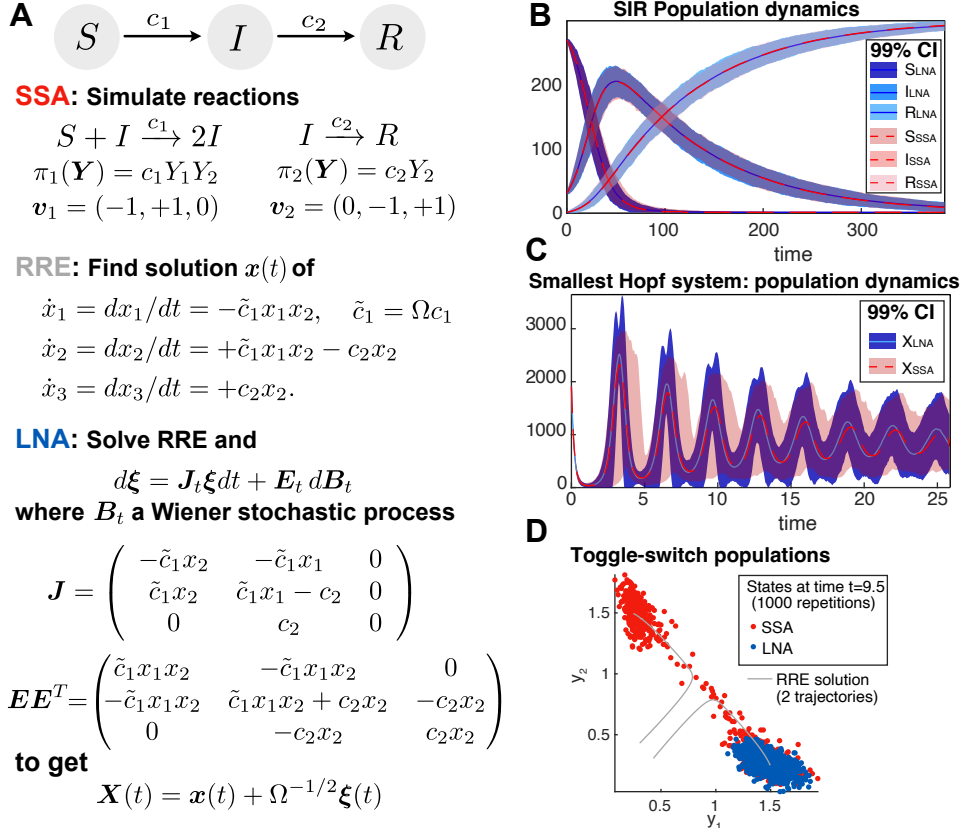


Figure 2: LNA method summary. A. LNA is a stochastic approximation of the stochastic population dynamics that can be exactly simulated using the SSA. LNA uses the numerical solutions of the deterministic RRE and a SDE that can be solved exactly. The SIR population dynamics model is used here as an example. B. Comparison between SSA and LNA on the SIR population dynamics in terms of simulated 99% Confidence Intervals (CI) shows astonishing agreement. C. In contrast, same comparisons between the LNA and SSA in one of the three species of the oscillatory system in [63] show significant discrepancies. D. Significant discrepancies are also observed for the same comparisons on the bistable Genetic Toggle-Switch system in [12].

systems, this is indeed the case. For instance, it is shown in [41] that this is true for systems with RRE that has an attractive limit cycle solution and a range of moderate system sizes. We adopt the term used in [41] to name this modelling technique, called Phase-Corrected Linear Noise Approximation (pcLNA).

2.4 The phase corrected Linear Noise Approximation (pcLNA)

Here we present the phase corrected Linear Noise Approximation (LNA) algorithm for simulating reaction networks with non-linear dynamics using LNA transitions. For each $t \geq 0$, we define the pcLNA ansatz;

$$\mathbf{X}(t) = \mathbf{x}(t) + \Omega^{-1/2} \boldsymbol{\xi}(t) = G(\mathbf{X}(t)) + \Omega^{-1/2} \boldsymbol{\kappa}(t). \quad (14)$$

Here $G : \mathbb{R}^n \rightarrow \gamma$, $G(\mathbf{X}(t)) = \mathbf{x}(s)$, $s \geq 0$, is the phase correction function that maps any stochastic state $\mathbf{X}(t) \in \mathbb{R}^n$ to a point, say $\mathbf{x}(s) \in \gamma$, lying on a solution $\gamma = \{\mathbf{x}(t) : t \geq 0\}$ of the RRE in (6) that has the correct phase $s \geq 0$ for the current state $\mathbf{X}(t)$. The term $\boldsymbol{\kappa}(t)$ denotes the deviation of $\mathbf{X}(t)$ away from $\mathbf{x}(s) = G(\mathbf{X}(t))$. We use this ansatz to simulate stochastic trajectories as described in Algorithm 1.

Algorithm 1 General pcLNA algorithm

Inputs:

- a. Initial conditions: $s_0 = 0 = t_0$, $\mathbf{x}(0)$, $\mathbf{X}(0)$, Parameters: Δt , Ω .
- b. A solution $\gamma = \{\mathbf{x}(t) : t \geq 0\}$ of a RRE as in (6) and the corresponding solutions \mathbf{C} and \mathbf{D} of (12), (13), respectively.
- c. The phase correction map $G : \mathbb{R}^n \rightarrow \gamma$

Steps: Take $\boldsymbol{\kappa}(s_0) = \Omega^{1/2}(\mathbf{X}(0) - \mathbf{x}(0))$ and for $i = 1, 2, \dots$,

1. draw sample $\boldsymbol{\xi}(s_{i-1} + \Delta t)$ from the MVN distribution with mean $\mathbf{C}(s_{i-1}, s_{i-1} + \Delta t)\boldsymbol{\kappa}(s_{i-1})$, and variance matrix $\mathbf{D}(s_{i-1}, s_{i-1} + \Delta t)$;
2. compute $\mathbf{X}(t_i) = \mathbf{x}(s_{i-1} + \Delta t) + \Omega^{-1/2}\boldsymbol{\xi}(s_{i-1} + \Delta t)$;
3. set s_i such that $G(\mathbf{X}(t_i)) = \mathbf{x}(s_i)$
4. set $\boldsymbol{\kappa}(s_i) = \Omega^{1/2}(\mathbf{X}(t_i) - \mathbf{x}(s_i))$.

Outputs: $\{\mathbf{X}(t_i) : i = 0, 1, 2, \dots\}$.

The Algorithm 1 uses the standard LNA transition in steps 1-2 interrupted by phase correction maps in steps 3-4. The map G is used to find the correct (for a specific context) phase for $\mathbf{X}(t_i)$. After phase correction, the phase of the system is moved from $s_{i-1} + \Delta t$ to s_i , the deterministic state moved from $\mathbf{x}(s_{i-1} + \Delta t)$ to $\mathbf{x}(s_i)$ and the fluctuations $\boldsymbol{\xi}(s_{i-1} + \Delta t)$ are replaced with the remaining fluctuations after phase correction, $\boldsymbol{\kappa}(s_i)$. Providing Δt is not too large, phase drifts occurring in the next LNA transition will be small. Indeed, $\{\boldsymbol{\kappa}(s_i) : i \in \mathbb{N}_0\}$ should have uniformly bounded variance and remain sufficiently small for the LNA predictions to be valid over the short time intervals $[s_i, s_i + \Delta t)$, $i \in \mathbb{N}_0$. Importantly for computational efficiency is that the same solutions of ODEs (6), (12) and (13) are used in all steps. The fact that these ODEs only need to be solved once before any simulations, rapidly increases the computation speed. The steps are illustrated in Figure 3.

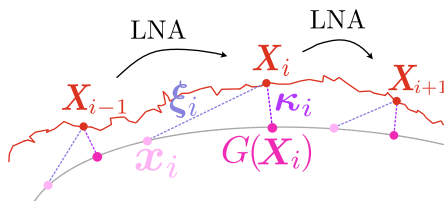


Figure 3: General pcLNA algorithm steps. pcLNA proceeds with standard LNA steps interrupted by phase corrections, $\mathbf{x}(t_i) \rightarrow G(\mathbf{X}(t_i)) = \mathbf{x}(s_i)$, and the related adjustments of the perturbation $\boldsymbol{\xi}(t_i) \rightarrow \boldsymbol{\kappa}(s_i)$.

All that is preventing one from readily following the steps in the pcLNA algorithm is the need for an explicit definition of the map G . A natural question arises: does a universal definition of

the map G exist that would apply to all reaction networks? As we will soon demonstrate, the answer is no; the concept of phase is inherently linked to the dynamics of the system's paths. Despite this, as will be discussed in the next section, the task of identifying G can be significantly simplified by utilizing results from the theory of dynamical systems.

2.5 The phase correction map

We use three connected concepts from the theory of dynamical systems to guide our approach in defining the phase correction map. The first concept is topological equivalence, which allows us to group various systems exhibiting the same type of dynamics. The second concept is decomposition, enabling us to break down complex (potentially high-dimensional) systems into their (possibly low-dimensional) non-linear component and linear components. This reduction simplifies the challenges associated with studying these systems in general, and specifically the definition of the phase correction map. The third concept involves the existence of exemplar systems within each group that are well understood and can serve as useful references. In the following sections, we will elaborate on these three concepts and explain how we practically apply them in the construction of phase correction maps. We will then apply them to define a map that works for *all* systems presenting a Hopf bifurcation and a different map that works for *all* systems exhibiting bistability through a fold bifurcation.

2.5.1 Topological equivalence

Topological equivalence between two continuous dynamical systems of the form (6) implies that the dynamics of the two systems are qualitatively identical. This is ensured by showing the existence of a homeomorphism² linking their parameter spaces and an associated parameter-dependent homeomorphisms mapping orbits of one system to the orbits of the other system, preserving the direction of time. When topological equivalence occurs locally, i.e. in respective neighborhoods of the domains of the two systems, then we say that the two systems are locally topologically equivalent (l.t.e.) in those neighborhoods (see Definitions 2.14-5 in [34], or SI section S3).

A practical approach to identify l.t.e. between dynamical systems is to examine the eigenvalues of their Jacobian matrix near an equilibrium point. To expand on this, we introduce some terminology. Suppose that a system of the form (6) has an equilibrium point, $(\mathbf{x}_{\alpha_p}, \alpha_p)$, i.e. $F(\mathbf{x}_{\alpha_p}, \alpha_p) = \mathbf{0}$. Let n_0 , n_+ , and n_- be the number of eigenvalues of the Jacobian matrix $\mathbf{J}(\mathbf{x}_{\alpha_p}, \alpha_p)$ that have zero, positive, and negative real part. An equilibrium is hyperbolic if $n_0 = 0$ and non-hyperbolic otherwise. For two systems that each have a hyperbolic equilibrium, l.t.e. near their respective equilibria is secured if they have identical values of n_+ and n_- (see Theorem 2.2 in [34]). Establishing l.t.e. near a non-hyperbolic equilibrium is more complicated but it can be achieved in some cases, as discussed below.

2.5.2 Decomposition

Near a non-hyperbolic equilibrium, all orbits of a system, as in (6), either lie on or converge (either as $t \rightarrow \infty$ or $t \rightarrow -\infty$) to an n_0 -dimensional manifold, known as the centre manifold. This centre manifold is tangent to the hyperplane that contains all the eigenvectors corresponding to the n_0 eigenvalues with zero real part (see Theorem 5.1 and Lemma 5.1 in [34] or SI section S3).

²a continuous bijective function between topological spaces

Moreover, a system as in (6) with a non-hyperbolic equilibrium $(\mathbf{x}_{\alpha_p}, \alpha_p)$ is l.t.e. to the following system;

$$\begin{cases} \dot{\mathbf{u}} = \mathbf{A}\mathbf{u} + \mathbf{g}(\mathbf{u}, \mathbf{V}_\alpha(\mathbf{u})), \\ \dot{\mathbf{v}} = -\mathbf{v}, \\ \dot{\mathbf{w}} = \mathbf{w}, \end{cases} \quad (15)$$

near $(\mathbf{x}_{\alpha_p}, \alpha_p)$. Here $\mathbf{u} \in \mathbb{R}^{n_0}$, $\mathbf{v} \in \mathbb{R}^{n_+}$, $\mathbf{w} \in \mathbb{R}^{n_+}$ are coordinates corresponding to the eigenbasis and \mathbf{A} is an $n_0 \times n_0$ matrix with all its eigenvalues, for $\alpha = \alpha_p$, having zero real part and $\mathbf{g} : \mathbb{R}^n \rightarrow \mathbb{R}^{n_0}$ is a smooth function with Taylor expansions starting with at least quadratic terms. The centre manifold is defined by $\mathbf{V}_\alpha(\mathbf{u})$ in the sense that points $(\mathbf{u}, \mathbf{v}, \mathbf{w})$ lie on the manifold if and only if they satisfy $(\mathbf{v}, \mathbf{w}) = \mathbf{V}_\alpha(\mathbf{u})$ (see Theorem 5.4 in [34], [52] or SI section S3).

We can always compute the decomposition $\mathbf{J}(\mathbf{x}_\alpha, \alpha) = \mathbf{R}^T \mathbf{\Lambda} \mathbf{R}$ where $\mathbf{\Lambda}$ the Jordan canonical form of $\mathbf{J}(\mathbf{x}_\alpha, \alpha)$ and specify coordinates $(\mathbf{u}, \mathbf{v}, \mathbf{w})^T = \mathbf{R}^T(\mathbf{x} - \mathbf{x}_\alpha)$. Then we can use the $n \times n_0$ matrix, say \mathbf{R}_1 , with n_0 columns corresponding to the n_0 eigenvalues with zero real part when $\alpha = \alpha_p$ to derive a vector of \mathbf{u} -coordinates of the orbits lying on the centre manifold. That is, take a long term orbit $\gamma = \{\mathbf{x}(t) : t \geq 0\}$ near the equilibrium \mathbf{x}_α of the system in (6). The orbit γ will either lie on or quickly converge to the centre manifold of (6) emerging near $(\mathbf{x}_{\alpha_p}, \alpha_p)$. Then for $\mathbf{x} \in \gamma$, $\mathbf{u} = \mathbf{R}_1^T(\mathbf{x} - \mathbf{x}_\alpha)$ is a \mathbf{u} coordinate, as in (15), of a centre manifold satisfying an equation of the form $(\mathbf{v}, \mathbf{w}) = \mathbf{V}_\alpha(\mathbf{u})$. This provides a practical way for finding \mathbf{u} -coordinates for orbits lying on the centre manifold near a non-hyperbolic equilibrium of a system as in (6).

2.5.3 Normal forms

It is helpful, but not necessary, for the specification of the phase correction map of a class of l.t.e. systems, to identify a simple exemplar system in this class. We call normal forms the simplest systems in a class of l.t.e. systems. The normal forms of low dimensional centre manifolds are well studied. Characteristic examples include the fold, and Hopf bifurcations (see [34], and Figure 4).

Normal forms are useful in two ways. First, they specify the conditions under which a system is locally topologically equivalent (l.t.e.) to them. These conditions are often related to the eigen-decomposition of the Jacobian matrix in (7) at a non-hyperbolic equilibrium. This provides a practical, and often straightforward, method for determining whether a system belongs to a particular class. Secondly, their simpler form makes it easier to identify the key qualitative features (e.g., oscillations, multi-stability) shared by systems in that class, and to guide the choice of an appropriate phase correction map.

2.5.4 Consequences for phase correction

We proceed with the following actions based on the results obtained:

1. The concept of topological equivalence enables us to categorize different systems that exhibit qualitatively identical dynamics in the vicinity of an equilibrium point. We will employ the same form of phase correction map for each group of such systems.
2. The principle of decomposition allows us to construct a set of coordinates for a system where its non-linear dynamics are expressed. Given that phase drifts are relevant only to non-linear dynamics, we will apply phase correction to these particular coordinates.
3. The idea of normal forms helps us to determine whether a specific system belongs to a recognised class of systems with qualitatively identical dynamics near an equilibrium.

Supercritical Hopf Bifurcation

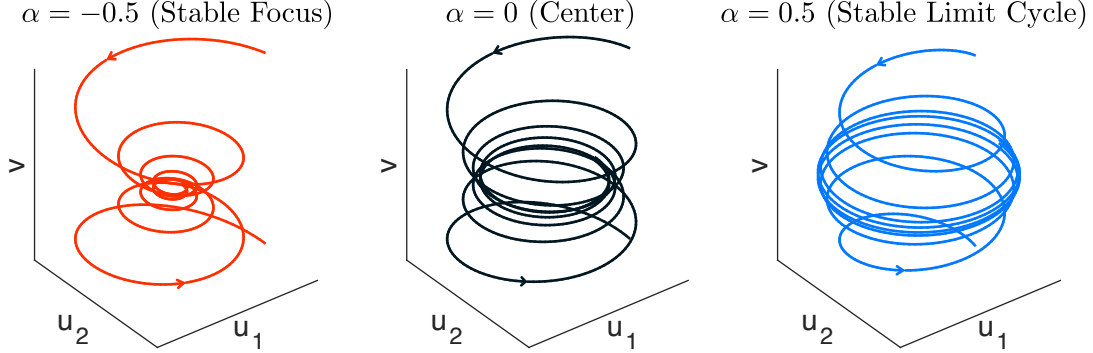


Figure 4: The dynamics of a generic normal form of the supercritical Hopf bifurcation. The two-dimensional centre manifold has coordinate $\mathbf{u} = (u_1, u_2)$, while the third coordinate v satisfies $\dot{v} = -v$. Selected orbits for the three different cases are presented.

Furthermore, it allows us to study the characteristics of these classes (e.g., oscillations, multi-stabilities) to select appropriate phase correction maps.

2.5.5 Generalised pcLNA

First, we make the observation that, while the Algorithm 1 uses a single deterministic trajectory $\gamma = \{\mathbf{x}(t) : t \geq 0\}$, some classes of systems prompt the need for using more than one trajectory. This is particularly the case for systems presenting more than one stable equilibria in nearby locations (see Figure 2D and section 4). The generalised pcLNA algorithm in 2 allows for a phase correction function that maps a stochastic state \mathbf{X} to a point lying on one of a set of deterministic trajectories $\gamma^{(j)} = \{\mathbf{x}^{(j)}(t) : t \geq 0\}$, $j = 1, 2, \dots, J$, that all satisfy the system in (6) and differ only on their initial conditions, $\mathbf{x}^{(j)}(0)$. It is clear that Algorithm 1 is a special case of Algorithm 2 for $J = 1$.

Algorithm 2 Generalised pcLNA algorithm

Inputs:

- Initial conditions: $s_0 = 0 = t_0$, j_0 , $\mathbf{X}(0)$, $\mathbf{x}^{(j)}(0)$, $j = 1, \dots, J$. Parameters: Δt , Ω .
- Solutions $\gamma^{(j)} = \{\mathbf{x}^{(j)}(t) : t \geq 0\}$, $j = 1, 2, \dots, J$ of a RRE as in (6) and the corresponding solutions $\mathbf{C}^{(j)}$ and $\mathbf{D}^{(j)}$ of (12), (13), respectively.
- The phase correction map $G : \mathbb{R}^n \rightarrow \{\gamma^{(j)} : j = 1, \dots, J\}$

Steps: Take $\boldsymbol{\kappa}(s_0) = \Omega^{1/2}(\mathbf{X}(0) - \mathbf{x}^{(j_0)}(0))$ and for $i = 1, 2, \dots$,

- draw sample $\boldsymbol{\xi}(s_{i-1} + \Delta t)$ from the MVN distribution with mean $\mathbf{C}(s_{i-1}, s_{i-1} + \Delta t)\boldsymbol{\kappa}(s_{i-1})$, and variance matrix $\mathbf{D}(s_{i-1}, s_{i-1} + \Delta t)$;
- compute $\mathbf{X}(t_i) = \mathbf{x}^{(j_{i-1})}(s_{i-1} + \Delta t) + \Omega^{-1/2}\boldsymbol{\xi}(s_{i-1} + \Delta t)$;
- set (j_i, s_i) such that $G(\mathbf{X}(t_i)) = \mathbf{x}^{(j_i)}(s_i)$, $j_i \in \{1, \dots, J\}$;
- set $\boldsymbol{\kappa}(s_i) = \Omega^{1/2}(\mathbf{X}(t_i) - \mathbf{x}(s_i))$.

Outputs: $\{\mathbf{X}(t_i) : i = 0, 1, 2, \dots\}$.

2.5.6 Defining the phase correction map

Recall that we wish to define the phase correction map G to take any stochastic state \mathbf{X} and map it to a point on a deterministic evolution of the system described in (6). The results in Section 2.5.4 suggest phase correction maps that are specific to each class of qualitatively identical (that is, l.t.e.) dynamics, and apply phase correction on the non-linear coordinates of the system using a suitable map for the type of dynamics presented on exemplar systems in the class.

This translates to the following general steps for defining a phase correction map G for any stochastic state \mathbf{X} :

1. Suppose that a RRE system as in (6) has a non-hyperbolic equilibrium, $(\mathbf{x}_{\alpha_p}, \alpha_p)$. That is, $\mathbf{F}(\mathbf{x}_{\alpha_p}, \alpha_p) = \mathbf{0}$, and the Jacobian matrix $\mathbf{J}(\mathbf{x}_{\alpha_p}, \alpha_p)$ has n_0 ($n_0 > 0$) eigenvalues with zero real part.
2. Identify the class of systems that the RRE system belongs to by checking whether it satisfies certain conditions such as those described in Sections 3 and 4.
3. For α in the vicinity of α_p , solve the RRE system to derive trajectories $\gamma^{(j)} = \{\mathbf{x}^{(j)}(t) : t \geq 0\}$, $j = 1, 2, \dots, J$.
4. Define a projection map $\text{proj} : \mathbb{R}^n \rightarrow \mathbb{R}^{n_0}$, $\mathbf{u} = \text{proj}(\mathbf{x}) = \mathbf{R}_1^T (\mathbf{x} - \mathbf{x}_\alpha)$, where \mathbf{R}_1 a $n \times n_0$ matrix with columns an eigenbasis corresponding to the n_0 eigenvalues of $\mathbf{J}(\mathbf{x}_\alpha, \alpha)$ that for $\alpha = \alpha_p$ have zero real part.
5. Compute $\{\mathbf{u}^{(j)}(t) : t \geq 0\}$, where $\mathbf{u}^{(j)}(t) = \text{proj}(\mathbf{x}^{(j)}(t))$ that are \mathbf{u} -coordinates of the trajectories $\{\mathbf{x}^{(j)}(t) : t \geq 0\}$, $j = 1, \dots, J$, and $\mathbf{U} = \text{proj}(\mathbf{X})$
6. Find

$$(j, s) = \underset{l \in \{1, \dots, J\}, t \geq 0}{\text{argmin}} \|\mathbf{U} - \mathbf{u}^{(l)}(t)\| \quad (16)$$

7. Define $G : \mathbb{R}^n \rightarrow \{\gamma^{(j)} : j = 1, \dots, J\}$, where

$$G(\mathbf{X}) = \mathbf{x}^{(j)}(s). \quad (17)$$

We chose to use the Euclidean distance $\|\cdot\|$ in (16) for its simplicity and speed of computation, but the method can be applied using other distance metrics. Figure 5 illustrate steps (5-7) above.

3 Hopf bifurcation systems

We now consider systems which present oscillatory behaviour. In particular, we wish to draw a stochastic trajectory $\{\mathbf{X}(t_i) : i = 0, 1, 2, \dots\}$, with $\mathbf{X}(t_i) \in \mathbb{R}^n$ for a reaction network with macroscopic RRE as in (6) and Jacobian $\mathbf{J}(\mathbf{x}, \alpha)$ as in (7) that satisfy the following conditions:

- (H.I) there exists an $\alpha_p \in \mathbb{R}$ and $\mathbf{x}_{\alpha_p} \in \mathbb{R}^n$ such that, $\mathbf{F}(\mathbf{x}_{\alpha_p}, \alpha_p) = \mathbf{0}$,
- (H.II) for α local to α_p , all the eigenvalues of the Jacobian matrix, $\mathbf{J}(\mathbf{x}_\alpha, \alpha)$ are negative except for a pair of complex conjugate eigenvalues $\lambda(\alpha)$, $\bar{\lambda}(\alpha)$ such that

$$\lambda(\alpha) = \mu(\alpha) + i\omega(\alpha), \quad \text{where} \quad \mu(\alpha_p) = 0, \quad \omega(\alpha_p) > 0.$$

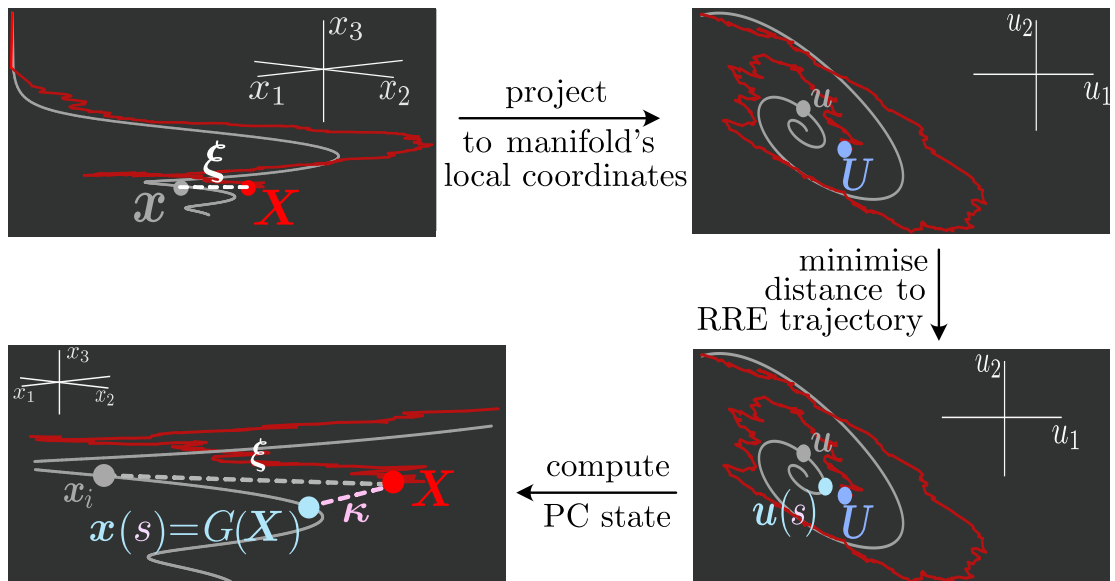


Figure 5: Phase correction. The phase correction $G(\mathbf{X}_i)$ for a point \mathbf{X}_i on the stochastic trajectory is computed in three steps. First, the RRE solution and point \mathbf{X}_i is projected into the \mathbf{u} -coordinates of the non-linear Centre manifold. Then, the point, $\mathbf{u}(s_i)$ lying on the projected RRE trajectory $\{\mathbf{u}(t) : t \geq 0\}$ that minimises the distance to \mathbf{U}_i is found. Finally, the corresponding point, $\mathbf{x}(s_i)$, with the same time-point s_i with $\mathbf{u}(s_i)$ and that lies on the RRE solution $\{\mathbf{x}(t) : t \geq 0\}$ is found. The point $\mathbf{x}(s_i)$ and the perturbation $\boldsymbol{\kappa}_i$ (instead of \mathbf{x}_i and $\boldsymbol{\xi}_i$) are used in the next LNA transition. The magnitude of $\boldsymbol{\kappa}_i$ is smaller or equal than the magnitude of $\boldsymbol{\xi}_i$ on the \mathbf{u} -coordinates.

Condition (H.I) is precisely the requirement for the macroscopic reaction rate equation to exhibit an equilibrium. Condition (H.II) ensures the equilibrium is non-hyperbolic and therefore prescribes the existence of a parameter dependent, two-dimensional, attracting manifold near $(\mathbf{x}_{\alpha_p}, \alpha_p)$ that is l.t.e. to a system of the form as in (15). Furthermore, the complex pair of eigenvalues of the Jacobian matrix implies that, near $(\mathbf{x}_{\alpha_p}, \alpha_p)$, the system is l.t.e. to the Generic Hopf bifurcation system (see Figure 4).

3.1 The pLNA algorithm for Hopf bifurcation systems

We now wish to define the phase correction map G for a reaction network with macroscopic RRE as in (6) satisfying conditions (H.I), (H.II). Consider some value α of the bifurcation parameter that is near the critical α_p and suppose that \mathbf{x}_α is an equilibrium for this value of the bifurcation parameter, i.e. $\mathbf{F}(\mathbf{x}_\alpha, \alpha) = \mathbf{0}$. Consider also a deterministic trajectory $\gamma = \{\mathbf{x}(t) : t \geq 0\}$ near \mathbf{x}_α . We wish to define the phase map $G : \mathbb{R}^n \rightarrow \gamma$ for any stochastic state $\mathbf{X} \in \mathbb{R}^n$.

First, we find the \mathbf{u} coordinates in (28). We identify the conjugate pair of eigenvectors, $\mathbf{u}_1 \pm i\mathbf{u}_2$, corresponding to the complex eigenvalues of the Jacobian $\mathbf{J}(\mathbf{x}_\alpha, \alpha)$. The eigenspace corresponding to these complex eigenvalues is spanned by $\{\mathbf{u}_1, \mathbf{u}_2\}$, and while the vectors $\mathbf{u}_1, \mathbf{u}_2$ are not necessarily orthonormal, we can easily find an orthonormal basis $\{\hat{\mathbf{u}}_1, \hat{\mathbf{u}}_2\}$ of this eigenspace using Gram-Schmidt orthonormalisation or a similar method. Letting $\mathbf{R}_1 = [\hat{\mathbf{u}}_1 \ \hat{\mathbf{u}}_2]$ we define

the map $\text{proj} : \mathbb{R}^n \rightarrow \mathbb{R}^2$, $\mathbf{u} = \text{proj}(\mathbf{x}) = \mathbf{R}_1^T(\mathbf{x} - \mathbf{x}_\alpha)$. We use the projection map to derive the \mathbf{u} -coordinates for the deterministic trajectory γ , $\{\mathbf{u}(t) : t \geq 0\}$ with $\mathbf{u}(t) = \text{proj}(\mathbf{x}(t))$, and for any stochastic state \mathbf{X} , $\mathbf{U} = \text{proj}(\mathbf{X})$.

As discussed in section 2.5.6, to control phase drifts we need to control the deviations of the stochastic trajectory in the \mathbf{u} coordinates. We therefore wish to minimise the distance of any stochastic states \mathbf{U} to $\{\mathbf{u}(t) : t \geq 0\}$. We define the map $\mathcal{M} \rightarrow \mathbb{R}^2 \in (0, \infty)$, where $s = \mathcal{M}(\mathbf{U}) = \text{argmin}_{t \geq 0} \|\mathbf{U} - \mathbf{u}(t)\|$, that gives the value of time t minimising the distance between \mathbf{U} and γ . Finally, the map $\mathbf{x} : (0, \infty) \rightarrow \gamma$, $\mathbf{x} = \mathbf{x}(s) \in \gamma$ simply lifts back the state $\mathbf{u}(s)$ to its original coordinates. The phase correction map G is the convolution $G = \mathbf{x} \circ \mathcal{M} \circ \text{proj}$, $\mathbf{x}(s) = G(\mathbf{X}) = \mathbf{x}(\mathcal{M}(\text{proj}(\mathbf{X})))$. The perturbation $\boldsymbol{\kappa}(t) = \sqrt{\Omega}(\mathbf{X}(t) - G(\mathbf{X}(t)))$ has minimised \mathbf{u} coordinate (see Figure 6).

Having defined the map G , we provide the pcLNA algorithm for Hopf bifurcation systems in Algorithm 3.

Algorithm 3 pcLNA for Hopf bifurcation systems

Inputs:

- a.. Initial conditions: $s_0 = 0 = t_0$, $\mathbf{x}(0)$, $\mathbf{X}(0)$, Parameters: Δt , Ω .
- b. System satisfying (H.I), (H.II), with solution $\gamma = \{\mathbf{x}(t) : t \geq 0\}$ and the corresponding solutions \mathbf{C} and \mathbf{D} of (12), (13), respectively.
- c. The projection map $\text{proj} : \mathbb{R}^n \rightarrow \mathbb{R}^2$, $\mathbf{u} = \text{proj}(\mathbf{x}) = \mathbf{R}_1^T(\mathbf{x} - \mathbf{x}_\alpha)$ where $\mathbf{R}_1 = [\hat{\mathbf{u}}_1 \ \hat{\mathbf{u}}_2]$ with $\hat{\mathbf{u}}_1$, $\hat{\mathbf{u}}_2$ an eigenbasis corresponding to the conjugate pair of complex eigenvalues of $\mathbf{J}(\mathbf{x}_\alpha, \alpha)$, and \mathbf{x}_α such that $\mathbf{F}(\mathbf{x}_\alpha, \alpha) = \mathbf{0}$.

Steps: Compute $\{\mathbf{u}(t) : t \geq 0\}$, where $\mathbf{u}(t) = \text{proj}(\mathbf{x}(t))$ and $\boldsymbol{\kappa}(s_0) = \Omega^{1/2}(\mathbf{X}(0) - \mathbf{x}(0))$.

For $i = 1, 2, \dots$,

1. draw sample $\boldsymbol{\xi}(s_{i-1} + \Delta t)$ from the MVN distribution with mean $\mathbf{C}(s_{i-1}, s_{i-1} + \Delta t)\boldsymbol{\kappa}(s_{i-1})$, and variance matrix $\mathbf{D}(s_{i-1}, s_{i-1} + \Delta t)$;
2. compute $\mathbf{X}(t_i) = \mathbf{x}(s_{i-1} + \Delta t) + \Omega^{-1/2}\boldsymbol{\xi}(s_{i-1} + \Delta t)$;
3. compute $\mathbf{U}_i = \text{proj}(\mathbf{X}(t_i))$, and find $s_i = \mathcal{M}(\mathbf{U}_i) = \text{argmin}_{t \geq 0} \|\mathbf{U}_i - \mathbf{u}(t)\|$.
4. compute $\boldsymbol{\kappa}(s_i) = \Omega^{1/2}(\mathbf{X}(t_i) - \mathbf{x}(s_i))$.

Outputs: $\{\mathbf{X}(t_i) : i = 0, 1, 2, \dots\}$.

4 Bi-stable systems

We now consider systems that present bi-stability. We focus on the type of bi-stability arising in the systems presented in [2], [19] and [12]. We wish to derive stochastic trajectories $\{\mathbf{X}(t_i) : i = 0, 1, 2, \dots\}$, with $\mathbf{X}(t_i) \in \mathbb{R}^n$, for a reaction network with RRE limit (as $\Omega \rightarrow \infty$) satisfying (6) and Jacobian, $\mathbf{J}(\mathbf{x}, \alpha)$, as in (7) that satisfy the conditions:

- (B.I) there exists an $\alpha_p \in \mathbb{R}$ and $\mathbf{x}_{\alpha_p} \in \mathbb{R}^n$ such that $\mathbf{F}(\mathbf{x}_{\alpha_p}, \alpha_p) = \mathbf{0}$;
- (B.II) all the eigenvalues of the Jacobian matrix $\mathbf{J}(\mathbf{x}_{\alpha_p}, \alpha_p)$ are negative except for one zero eigenvalue.
- (B.III) for α near $\alpha_p \in \mathbb{R}$ there exist $\mathbf{x}_1^* \in \mathbb{R}^n$ such that $\mathbf{F}(\mathbf{x}_1^*, \alpha) = \mathbf{0}$ and all the eigenvalues of the Jacobian matrix $\mathbf{J}(\mathbf{x}_1^*, \alpha)$ are negative.

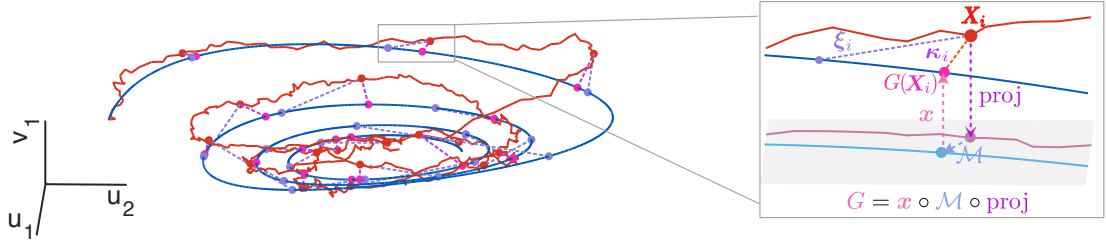


Figure 6: Phase correction (PC) for Hopf bifurcation systems. (Left) The stochastic trajectory (red) and deterministic trajectory (blue) in coordinates (\mathbf{u}, v_1) are displayed. The stochastic state (red circle) and the perturbations before (ξ , purple, dashed line) and after (κ , pink, dashed line) PC are displayed. (Right) Zoom in of a PC with the G map analysed as a convolution of the projection (proj), distance minimisation (\mathcal{M}), and lift back to original coordinates (\mathbf{x}) functions.

The last condition (B.III) ensures the presence of a stable equilibrium point for all values of α near $\alpha_p \in \mathbb{R}$. The conditions (B.I-II) prescribe the presence of a non-hyperbolic equilibrium, \mathbf{x}_{α_p} , and the existence of a parameter dependent, one-dimensional, attracting manifold near $(\mathbf{x}_{\alpha_p}, \alpha_p)$ that is l.t.e. to a system of the form as in (15). Furthermore, the same conditions imply that, near $(\mathbf{x}_{\alpha_p}, \alpha_p)$, the system is l.t.e. to the Generic Fold bifurcation system. For the Generic Fold bifurcation system, the non-hyperbolic equilibrium present at α_p disappears for $\alpha < \alpha_p$ while two equilibrium points, one stable and one unstable, emerge for $\alpha > \alpha_p$.

Therefore, a system satisfying the conditions (B.I-III) presents two stable and one unstable equilibrium points for $\alpha > \alpha_p$. That is, we arrive to the following result.

Remark 1 (Bistability). For a system as in (6) satisfying the conditions (B.I)-(B.III), with value of α such that $\alpha - \alpha_p$ is positive and sufficiently small, there exist $\mathbf{x}_1^*, \mathbf{x}_\alpha, \mathbf{x}_2^* \in \mathbb{R}^n$ with $\mathbf{F}(\mathbf{x}_1^*, \alpha) = \mathbf{F}(\mathbf{x}_\alpha, \alpha) = \mathbf{F}(\mathbf{x}_2^*, \alpha) = \mathbf{0}$ and all the eigenvalues of the Jacobian matrices $\mathbf{J}(\mathbf{x}_1^*, \alpha)$ and $\mathbf{J}(\mathbf{x}_2^*, \alpha)$ are negative (linear stability), while $\mathbf{J}(\mathbf{x}_\alpha, \alpha)$ has one positive eigenvalue (instability) and the rest are negative.

As mentioned above, we observe this type of bi-stability for the systems in [2], [19] and [12].

4.1 The pLNA algorithm for bi-stable systems

Following the pLNA principle, we construct a phase correction map G to control phase drifts for systems satisfying these conditions. As discussed in section 2.3.1, the LNA is long-time accurate when the system is in the vicinity of a stable equilibrium. This is the case for $\alpha \leq \alpha_p$. For the case where there is bi-stability, that is when $\alpha > \alpha_p$, the standard LNA that uses a single deterministic solution to simulate a trajectory will produce trajectories centered around the “nearest” equilibrium and therefore it will fail when there is a significant likelihood that a stochastic trajectory produced by SSA escapes from the nearest equilibrium (see Figure 2(D) and SI Figure S19). The main focus of phase correction is therefore to allow for this event. At the very least, more than one deterministic trajectories will need to be used.

There is a simple way to predict the equilibrium that the current state is expected to converge. If $\mathbf{R}_1 = \mathbf{u}$ is the eigenvector corresponding to the eigenvalue of $\mathbf{J}(\mathbf{x}_\alpha, \alpha)$ which is zero when $\alpha = \alpha_p$, then we define the projection map $\text{proj} : \mathbb{R}^n \rightarrow \mathbb{R}$, giving the u -coordinate $u = \text{proj}(\mathbf{x}) = \mathbf{R}_1(\mathbf{x} - \mathbf{x}_\alpha)$. The u -coordinates of the two stable equilibria, $u_1^* = \text{proj}(\mathbf{x}_1^*)$ and $u_2^* = \text{proj}(\mathbf{x}_2^*)$, have different sign, say $u_1^* < 0 < u_2^*$. Furthermore, near \mathbf{x}_α , the eigenvector \mathbf{u} defines a separatrix, that is the trajectories with initial condition that has negative (positive) u -coordinate converge to \mathbf{x}_1^* (\mathbf{x}_2^*).

The phase map $G(\mathbf{X})$ for a state \mathbf{X} of the stochastic trajectory is chosen to control perturbations in the u -coordinate. For this, it is essential that $G(\mathbf{X})$ and \mathbf{X} have u -coordinate of the same sign. We consider a phase map that uses two trajectories $\gamma_1 = \{\mathbf{x}^{(1)}(t) : t \geq 0\}$ and $\gamma_2 = \{\mathbf{x}^{(2)}(t) : t \geq 0\}$, the first converging to \mathbf{x}_1^* and the second to \mathbf{x}_2^* and their corresponding u -coordinates are $\{u^{(j)}(t) : t \geq 0\}$ with $u^{(j)}(t) = \text{proj}(\mathbf{x}^{(j)}(t))$, $j = 1, 2$. Let $U = \text{proj}(\mathbf{X})$. The phase map is then $G(\mathbf{X}) = \mathbf{x}_j(s)$, where $j \in \{1, 2\}$ satisfies $u_j^* U > 0$ (i.e. U and u_j^* have the same sign) and $s = \text{argmin}_{t \geq 0} \|U - u_j(t)\|$. This phase map ensures that when the trajectory jumps from one side of the separatrix to the other, then the map also switches side. Using only two trajectories is the most minimal option; one may consider using more trajectories or using a new trajectory every time the state jumps to a different side of the separatrix, but this will be computationally more costly. In Algorithm 4, we describe the associated pcLNA simulation algorithm. In section 5, we show that this simple phase map is sufficient to achieve high levels of accuracy.

Algorithm 4 pcLNA for bistable systems

Inputs:

- a. Initial conditions: $s_0 = 0 = t_0$, $j_0 \in \{1, 2\}$, $\mathbf{X}(0)$, $\{\mathbf{x}^{(j)}(0) : j = 1, 2\}$. Parameters: Δt , Ω .
- b. System satisfying Remark 1 with solutions $\gamma_j = \{\mathbf{x}^{(j)}(t) : t \geq 0\}$ converging to \mathbf{x}_j^* , $j = 1, 2$, respectively, and their corresponding solutions $\mathbf{C}^{(j)}$ and $\mathbf{D}^{(j)}$ of (12), (13), respectively.
- c. The projection map $\text{proj} : \mathbb{R}^n \rightarrow \mathbb{R}$, $u = \text{proj}(\mathbf{x}) = \mathbf{R}_1^T(\mathbf{x} - \mathbf{x}_\alpha)$ where $\mathbf{R}_1 = \mathbf{u}$ with \mathbf{u} a normalised eigenvector corresponding to the eigenvalue of $\mathbf{J}(\mathbf{x}_\alpha, \alpha)$ that is equal to zero for $\alpha = \alpha_p$.

Steps: Compute $\{u^{(j)}(t) : t \geq 0\}$ where $u^{(j)}(t) = \text{proj}(\mathbf{x}^{(j)}(t))$ and $u_j^* = \text{proj}(\mathbf{x}_j^*)$, for $j = 1, 2$, and $\boldsymbol{\kappa}(s_0) = \Omega^{1/2}(\mathbf{X}(0) - \mathbf{x}^{(j_0)}(0))$. For $i = 1, 2, \dots$

1. draw sample $\boldsymbol{\xi}(s_{i-1} + \Delta t)$ from the MVN distribution with mean $\mathbf{C}(s_{i-1}, s_{i-1} + \Delta t)\boldsymbol{\kappa}(s_{i-1})$, and variance matrix $\mathbf{D}(s_{i-1}, s_{i-1} + \Delta t)$;
2. compute $\mathbf{X}(t_i) = \mathbf{x}(s_{i-1} + \Delta t) + \Omega^{-1/2}\boldsymbol{\xi}(s_{i-1} + \Delta t)$;
3. compute $U = \text{proj}(\mathbf{X}(t_i))$ and set $j_i \in \{1, 2\}$ such that $u_{j_i}^* U > 0$ and $s_i = \text{argmin}_{t \geq 0} \|U - u_{j_i}(t)\|$;
4. compute $\boldsymbol{\kappa}(s_i) = \Omega^{1/2}(\mathbf{X}(t_i) - \mathbf{x}^{(j_i)}(s_i))$.

Outputs: $\{\mathbf{X}(t_i) : i = 0, 1, 2, \dots\}$.

5 Numerical investigations

As mentioned in Section 2.3, the LNA boasts fast computation of distributions of the stochastic process $\{\mathbf{X}(t) : t \geq 0\}$ as it only demands solving a set of ODEs to derive the RRE solutions $\{\mathbf{x}^{(j)}(t) : t \geq 0\}$, $j = 1, \dots, J$ in (6) and the corresponding drift and diffusion matrix solutions, $\mathbf{C}^{(j)}$ and $\mathbf{D}^{(j)}$, of Eq. (12-13). Since the pcLNA algorithm also only requires such solutions, it also inherits its speed of simulation.

Next, we study the accuracy and computational efficiency of the pcLNA compared to the SSA. For this, we separately use SSA and pcLNA to produce a large number of long-time, stochastic trajectories and then compare their empirical probability distribution at various time-points. We perform this exercise for various systems, either presenting bi-stability or a Hopf bifurcation.

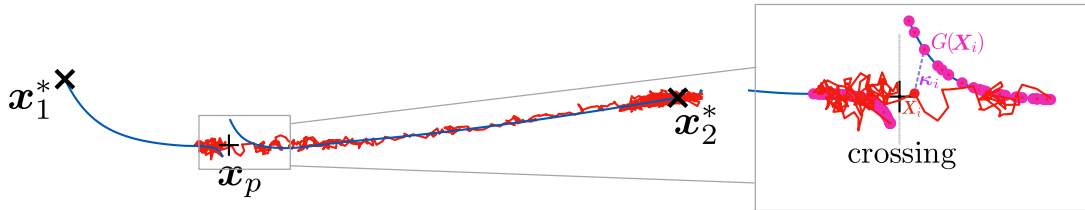


Figure 7: Phase Correction (PC) for bistable systems. (Left) The stochastic trajectory (red) and two deterministic trajectories (blue), each converging to a different stable equilibrium (x) on the two sides of the unstable equilibrium ($+$) are displayed. (Right) Zoom in to the part of simulation where a crossing from one side of the unstable equilibrium to the other was performed with the PC mapping G (pink circles) and the deviation κ_i shown.

For Hopf bifurcation systems, we perform comparisons for all three qualitatively different cases where the system complex conjugate pair of eigenvalues in (H.II) has $\mu(\alpha) < 0, = 0, > 0$. In these three cases, the limiting RRE system presents quickly dampened oscillations, slowly dampened oscillations, and sustained oscillations, respectively (see also Figure 1A and 4). For bistable systems, we focus on parameter values satisfying 1 (see Figure 1B, right) where the system present bistability.

The Hopf bifurcation systems used for comparisons are the following.

- The Brusselator system in [35], which is a classical oscillatory system involving complex interactions between two variables (for more details, see SI Section S4.2).
- The three-variable system in [63] that is the smallest reaction network presenting a Hopf bifurcation (see SI Section S4.3).
- The response of the NF- κ B signalling system to TNF α signals in [4], which is a system that involves 11 molecular populations involved in 24 reactions (see SI Section S4.1).

For the first two systems above, we produced 1000 stochastic trajectories using SSA and pcLNA for a time interval with length of 8τ , where τ the length of one period-cycle of the corresponding system. For the third system (where SSA simulations are substantially slower), we run 500 repetitions for a time-length of 4 periods of the system. We recorded the time taken to compute one stochastic trajectory for these time intervals, and then computed the median of these times, which we call CPU time in all the presented figures. We also collected using these simulations the state, $(X_1(t_j), \dots, X_n(t_j))$ of all variables at various time-points, $t_j, j = 1, 2, \dots, T$ in each repetition, and computed the corresponding empirical density functions for the probability distribution of each variable $X_i(t_j)$ using kernel density estimation in MATLAB [25]. We present the results in Figure 8A and SI Figures S9- S17.

We clearly see that the pcLNA and SSA distributions are hardly distinguishable, while the CPU time is reduced by a magnitude of order $O(10) - O(10^3)$. The reduction in CPU time depends on the complexity of the system (number and speed of reactions) and the system size. Larger system sizes imply larger number of reaction occurrences and slower SSA simulations, while CPU times for pcLNA are not affected by system size.

The bi-stable systems considered are the following.

- The Genetic Toggle-Switch system in [12], which involves two-variables (for more details, see SI Section S4.4).

- The two-variable, simplified Cell-Cycle system presented in [2] (see SI Section S4.5).
- The Somitogenesis Switch system, presented in [19], that involves four variables and ten reactions (see SI Section S4.6).

We produced 1000 trajectories using SSA and pcLNA for the above systems, running for time intervals of length sufficient for convergence to one of the two stable equilibria by the solution of the corresponding RRE.

Note that if we initialise the system at a point close to one of the stable equilibria, then nearly all trajectories converge to the same equilibrium and the SSA simulations are well approximated by the standard LNA. Instead, we focused on simulations where the initial conditions are close to the unstable equilibrium so that there is a substantial probability of convergence of a given stochastic trajectory for both equilibria. In this case, all the standard LNA trajectories will converge to the same equilibrium and therefore can badly fail to approximate the SSA simulations (see Figure 2(D) and SI Figure S19).

The pcLNA algorithm 4 requires the choice of at least two solutions of RRE that differ only by their initial condition and converge to a different equilibrium. In the presented simulations, the two initial conditions are of the form $(1 - \epsilon) \mathbf{x}_\alpha + \epsilon \mathbf{x}_j^* + \mathbf{c}$, $j = 1, 2$. Here $0 \leq \epsilon \leq 0.1$, \mathbf{x}_α the unstable equilibrium and \mathbf{x}_j^* , $j = 1, 2$, the stable equilibria. The real vector \mathbf{c} performs a change of location in a direction orthogonal to the eigenvector corresponding to the real positive eigenvalue of the Jacobian $\mathbf{J}(\mathbf{x}^u)$. This change of location allows to view some short-time transient dynamics, but it is not necessary if one is interested in the long-time dynamics. For the specific initial conditions and other details, see SI Sections S4.4- S4.6.

The results are presented in Figure 8B and SI Figures S18, S20, S21. The two methods, SSA and pcLNA, are compared in the same way as the Hopf bifurcation system and the results are again showing the agreement between the two methods and similarly to above, significant reductions in the CPU time, especially for the Somitogenesis Switch system (pcLNA CPU time is ≈ 58 times smaller) .

6 Discussion

The results in this paper demonstrate the capability of the modified LNA method to effectively capture non-linear dynamics over long time intervals. The accuracy of the approximation combined with the analytical tractability of the LNA method, and speed of computation establishes a robust framework for investigating population dynamics, and fitting these models to data. It overcomes key limitations of existing methods and opens new avenues for advancing the stochastic modeling of dynamical systems.

We showcase the versatility of our methodology across a range of systems exhibiting two fundamental forms of non-linear behavior—oscillations and bistability—which are common in biology and other scientific domains. Beyond these cases, our approach, grounded in center manifold theory from dynamical systems, is applicable to a much broader class of reaction networks. Specifically, for any network whose RRE solution features a non-hyperbolic equilibrium—a scenario frequently encountered in practice—the pcLNA algorithm enables fast and accurate simulation of long-term stochastic trajectories, even in large and complex systems.

Such stochastic simulations are essential for applications including in silico experimentation, and sensitivity analysis [30, 23, 59, 47, 37, 51, 7, 44], and statistical inference using Approximate Bayesian Computation methods [55, 40, 53, 57]. Moreover, this work lays the groundwork for future methods that leverage the long-term accuracy and analytical strengths of pcLNA—enabling, for instance, the exact computation of likelihood functions for time-series data, as well as key

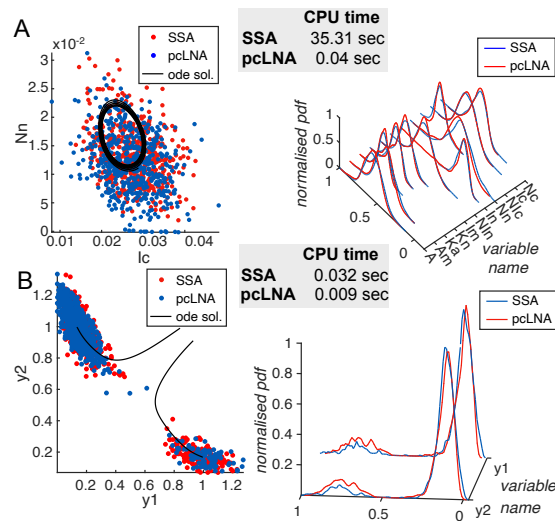


Figure 8: Comparison between SSA (red) and pcLNA (blue) for (A) the NF- κ B [4] and (B) the cell-cycle [2] system. (Left) The states recorded after four cycles (A) and at $t = 100$ mins (B) of respectively $n = 500$ and $n = 1000$ simulations of the two systems and solutions of the corresponding RRE in (6). (Right) The corresponding empirical probability density functions of each of the system variables. The median CPU times for deriving one stochastic trajectory are also reported. See SI Section S4 for the details of the simulations.

quantities like the Fisher Information, which are critical for assessing system sensitivity and robustness to parameter variation.

References

- [1] D.F. Anderson and T.G. Kurtz. *Continuous Time Markov Chain Models for Chemical Reaction Networks*, pages 3–42. Springer New York, 2011.
- [2] David Angeli, James E. Ferrell, and Eduardo D. Sontag. Detection of multistability, bifurcations, and hysteresis in a large class of biological positive-feedback systems. *Proceedings of the National Academy of Sciences*, 101:1822–1827, 2 2004.
- [3] Sol M. Fernández Arancibia, Hernán E. Grecco, and Luis G. Morelli. Effective description of bistability and irreversibility in apoptosis. *Phys. Rev. E*, 104:064410, Dec 2021.
- [4] L. Ashall, C.A. Horton, D.E. Nelson, P. Paszek, C.V. Harper, K. Sillitoe, S. Ryan, D.G. Spiller, J.F. Unitt, D.S. Broomhead, D.B. Kell, D.A. Rand, V. Sée, and M.R.H. White. Pulsatile stimulation determines timing and specificity of nf- κ b-dependent transcription. *Science (American Association for the Advancement of Science)*, 324(5924):242–246, 2009.
- [5] R.P. Boland, T. Galla, and A.J. McKane. How limit cycles and quasi-cycles are related in systems with intrinsic noise. *Journal of Statistical Mechanics: Theory and Experiment*, 2008, 9 2008.
- [6] Zhixing Cao and Ramon Grima. Linear mapping approximation of gene regulatory networks with stochastic dynamics. *Nature Communications*, 9:3305, 8 2018.

- [7] Harsh Chhajer and Rahul Roy. Rationalised experiment design for parameter estimation with sensitivity clustering. *Scientific Reports*, 14:25864, 10 2024.
- [8] Francis Corson and Eric Dean Siggia. Geometry, epistasis, and developmental patterning. *Proceedings of the National Academy of Sciences*, 109:5568–5575, 4 2012.
- [9] Mirela Domijan, Paul E. Brown, Boris V. Shulgin, and David A. Rand. Pettsy: a computational tool for perturbation analysis of complex systems biology models. *BMC Bioinformatics*, 17:124, 3 2016.
- [10] Bärbel Finkenstädt, Dan J. Woodcock, Michal Komorowski, Claire V. Harper, Julian R. E. Davis, Mike R. H. White, David a. Rand, Barbel Finkenstadt, Dan J. Woodcock, Michal Komorowski, Claire V. Harper, Julian R. E. Davis, Mike R. H. White, and David a. Rand. Quantifying intrinsic and extrinsic noise in gene transcription using the linear noise approximation: An application to single cell data. *The Annals of Applied Statistics*, 7:1960–1982, 12 2013.
- [11] Sorana Froda and Séverien Nkurunziza. Prediction of predator–prey populations modelled by perturbed odes. *Journal of Mathematical Biology*, 54(3):407–451, 2007.
- [12] Timothy S. Gardner, Charles R. Cantor, and James J. Collins. Construction of a genetic toggle switch in *escherichia coli*. *Nature*, 403:339–342, 1 2000.
- [13] D.T. Gillespie. A general method for numerically simulating the stochastic time evolution of coupled chemical reactions. *Journal of Computational Physics*, 22(4):403–434, 1976.
- [14] D.T. Gillespie. Exact stochastic simulation of coupled chemical reactions. *The Journal of Physical Chemistry*, 81(25):2340–2361, 1977.
- [15] D.T. Gillespie. A rigorous derivation of the chemical master equation. *Physica A*, 188(1):404–425, 1992.
- [16] D.T. Gillespie. The chemical Langevin equation. *The Journal of Chemical Physics*, 113(1):297–306, 07 2000.
- [17] D.T. Gillespie. Approximate accelerated stochastic simulation of chemically reacting systems. *The Journal of Chemical Physics*, 115(4):1716–1733, 07 2001.
- [18] D.T. Gillespie and L.R. Petzold. Improved leap-size selection for accelerated stochastic simulation. *The Journal of Chemical Physics*, 119(16):8229–8234, 10 2003.
- [19] Albert Goldbeter, Didier Gonze, and Olivier Pourquié. Sharp developmental thresholds defined through bistability by antagonistic gradients of retinoic acid and fgf signaling. *Developmental Dynamics*, 236:1495–1508, 6 2007.
- [20] Andrew Golightly, Laura E. Wadkin, Sam A. Whitaker, Andrew W. Baggaley, Nick G. Parker, and Theodore Kypraios. Accelerating bayesian inference for stochastic epidemic models using incidence data. *Statistics and Computing*, 33:134, 12 2023.
- [21] Didier Gonze, José Halloy, Jean-Christophe Leloup, and Albert Goldbeter. Stochastic models for circadian rhythms: effect of molecular noise on periodic and chaotic behaviour. *Comptes Rendus Biologies*, 326(2):189 – 203, 2003.
- [22] Theodore W. Grunberg and Domitilla Del Vecchio. A stein’s method approach to the linear noise approximation for stationary distributions of chemical reaction networks, 2024.

- [23] Ankit Gupta and Mustafa Khammash. An efficient and unbiased method for sensitivity analysis of stochastic reaction networks. *Journal of the Royal Society Interface*, 11:20140979–20140979, 2014.
- [24] A.V. Hill. The possible effects of the aggregation of the molecules of hæmoglobin on its dissociation curves. *The Journal of Physiology*, 40:i–vii, January 1910.
- [25] The MathWorks Inc. Matlab version: 9.13.0 (r2022b), 2023.
- [26] N. Ishii, K. Nakahigashi, T. Baba, M. Robert, T. Soga, A. Kanai, T. Hirasawa, M. Naba, K. Hirai, A. Hoque, P.Y. Ho, Y. Kakazu, K. Sugawara, S. Igarashi, S. Harada, T. Masuda, N. Sugiyama, T. Togashi, M. Hasegawa, Y. Takai, K. Yugi, K. Arakawa, N. Iwata, Y. Toya, Y. Nakayama, T. Nishioka, K. Shimizu, H. Mori, and M. Tomita. Multiple high-throughput analyses monitor the response of e. coli to perturbations. *Science (American Association for the Advancement of Science)*, 316(5824):593–597, 2007.
- [27] Y. Ito and K. Uchida. Formulas for intrinsic noise evaluation in oscillatory genetic networks. *Journal of Theoretical Biology*, 267:223–234, 11 2010.
- [28] Chen Jia and Ramon Grima. Holimap: an accurate and efficient method for solving stochastic gene network dynamics. *Nature Communications*, 15:6557, 8 2024.
- [29] K.A. Johnson and R.S. Goody. The original michaelis constant: Translation of the 1913 michaelis–menten paper. *Biochemistry (Easton)*, 50(39):8264–8269, 2011.
- [30] Michal Komorowski, Maria J Costa, David a Rand, and Michael P H Stumpf. Sensitivity, robustness, and identifiability in stochastic chemical kinetics models. *Proceedings of the National Academy of Sciences of the United States of America*, 108:8645–8650, 5 2011.
- [31] Michal Komorowski, Barbel Finkenstadt, Claire V Harper, David a Rand, Bärbel Finkenstädt, Claire V Harper, David a Rand, Barbel Finkenstadt, Claire V Harper, and David a Rand. Bayesian inference of biochemical kinetic parameters using the linear noise approximation. *BMC Bioinformatics*, 10:343, 10 2009.
- [32] T.G. Kurtz. Limit theorems for sequences of jump markov processes approximating ordinary differential processes. *Journal of Applied Probability*, 8(2):344–356, 1971.
- [33] T.G. Kurtz, Society for Industrial, and Applied Mathematics. *Approximation of Population Processes*. Number nos. 36-40 in *Approximation of Population Processes*. Society for Industrial and Applied Mathematics, 1981.
- [34] Y. Kuznetsov. *Elements of Applied Bifurcation Theory, 3rd Edic.* Society for Industrial and Applied Mathematics, 2011.
- [35] R. Lefever and G. Nicolis. Chemical instabilities and sustained oscillations. *Journal of Theoretical Biology*, 30(2):267–284, 1971.
- [36] Ioannis Lestas, Johan Paulsson, Nicholas E. Ross, and Glenn Vinnicombe. Noise in gene regulatory networks. *IEEE Transactions on Automatic Control*, 53:189–200, 1 2008.
- [37] Juliane Liepe, Paul Kirk, Sarah Filippi, Tina Toni, Chris P Barnes, and Michael P H Stumpf. A framework for parameter estimation and model selection from experimental data in systems biology using approximate bayesian computation. *Nature Protocols*, 9:439–456, 2 2014.

- [38] S. Mangan and U. Alon. Structure and function of the feed-forward loop network motif. *Proceedings of the National Academy of Sciences*, 100:11980–11985, 10 2003.
- [39] Elli Marinopoulou, Veronica Biga, Nitin Sabherwal, Anzy Miller, Jayni Desai, Antony D. Adamson, and Nancy Papalopulu. Hes1 protein oscillations are necessary for neural stem cells to exit from quiescence. *iScience*, 24:103198, 10 2021.
- [40] Paul Marjoram, John Molitor, Vincent Plagnol, and Simon Tavaré. Markov chain monte carlo without likelihoods. *Proceedings of the National Academy of Sciences*, 100:15324–15328, 12 2003.
- [41] G. Minas and D.A. Rand. Long-time analytic approximation of large stochastic oscillators: Simulation, analysis and inference. *PLoS Computational Biology*, 13, 7 2017.
- [42] G. Minas and D.A. Rand. Parameter sensitivity analysis for biochemical reaction networks. *Mathematical biosciences and engineering : MBE*, 16(5):3965–3987, 2019.
- [43] G. Minas, D.J. Woodcock, L. Ashall, C. Harper, M.R.H. White, and D.A. Rand. Multiplexing information flow through dynamic signalling systems. *PLoS computational biology*, 16(8):e1008076–e1008076, 2020.
- [44] Giorgos Minas and David A Rand. Parameter sensitivity analysis for biochemical reaction networks. *Mathematical Biosciences and Engineering*, 16:3965–3987, 4 2019.
- [45] Bela Novak and John J. Tyson. Numerical analysis of a comprehensive model of m-phase control in xenopus oocyte extracts and intact embryos. *Journal of Cell Science*, 106:1153–1168, 12 1993.
- [46] Joseph R. Pomerening, Sun Young Kim, and James E. Ferrell. Systems-level dissection of the cell-cycle oscillator: Bypassing positive feedback produces damped oscillations. *Cell*, 122:565–578, 8 2005.
- [47] Tom Rainforth, Adam Foster, Desi R. Ivanova, and Freddie Bickford Smith. Modern bayesian experimental design. *Statistical Science*, 39, 2 2024.
- [48] Nitzan Rosenfeld, Michael B Elowitz, and Uri Alon. Negative autoregulation speeds the response times of transcription networks. *Journal of Molecular Biology*, 323:785–793, 11 2002.
- [49] David Schnoerr, Guido Sanguinetti, and Ramon Grima. Approximation and inference methods for stochastic biochemical kinetics - a tutorial review. *Journal of Physics A: Mathematical and Theoretical*, 50, 8 2016.
- [50] M. Scott, B. Ingalls, and M. Kærn. Estimations of intrinsic and extrinsic noise in models of nonlinear genetic networks. *Chaos*, 16, 2006.
- [51] Ali Shahmohammadi and Kimberley B. McAuley. Using prior parameter knowledge in model-based design of experiments for pharmaceutical production. *AIChE Journal*, 66, 11 2020.
- [52] A. N. Shoshitaishvili. Bifurcations of topological type at singular points of parametrized vector fields. *Functional analysis and its applications*, 6(2):169–170, 1972.
- [53] S. A. Sisson, Y. Fan, and Mark M. Tanaka. Sequential monte carlo without likelihoods. *Proceedings of the National Academy of Sciences*, 104:1760–1765, 2 2007.

- [54] B. Swallow, D.A. Rand, and G. Minas. Bayesian inference for stochastic oscillatory systems using the phase-corrected linear noise approximation. *Bayesian Analysis*, pages 1 – 30, 2024.
- [55] Simon Tavaré, David J Balding, R C Griffiths, and Peter Donnelly. Inferring coalescence times from dna sequence data. *Genetics*, 145:505–518, 2 1997.
- [56] P. Thomas, H. Matuschek, and R. Grima. How reliable is the linear noise approximation of gene regulatory networks? *BMC Genomics*, 14, 2013.
- [57] Tina Toni, David Welch, Natalja Strelkowa, Andreas Ipsen, and Michael P.H Stumpf. Approximate bayesian computation scheme for parameter inference and model selection in dynamical systems. *Journal of The Royal Society Interface*, 6:187–202, 2 2009.
- [58] N.G. van Kampen. *Stochastic Processes in Physics and Chemistry*. Elsevier Science Publishers, Amsterdam, 1992.
- [59] Joep Vanlier, Christian A Tiemann, Peter AJ Hilbers, and Natal AW van Riel. Optimal experiment design for model selection in biochemical networks. *BMC Systems Biology*, 8:20, 2014.
- [60] P. Waage and C.M. Gulberg. Studies concerning affinity. *Journal of chemical education*, 63(12):1044–, 1986.
- [61] E.W.J. Wallace, D.T. Gillespie, K.R. Sanft, and L.R. Petzold. Linear noise approximation is valid over limited times for any chemical system that is sufficiently large. *IET Systems Biology*, 6:102–115, 8 2012.
- [62] Joshua S. Weitz, Sang Woo Park, Ceyhun Eksin, and Jonathan Dushoff. Awareness-driven behavior changes can shift the shape of epidemics away from peaks and toward plateaus, shoulders, and oscillations. *Proceedings of the National Academy of Sciences*, 117:32764–32771, 12 2020.
- [63] T. Wilhelm and R. Heinrich. Smallest chemical-reaction system with hopf-bifurcation. *J Math Chem*, 17:1–14, 1995.
- [64] Darren James Wilkinson. *Stochastic modelling for systems biology*, 2012.

Supporting Information (SI)

The SI contains further mathematical details and numerical investigations referenced in the main paper. We used PeTTSy [9] implemented in the MATLAB [25] environment and available at <https://wrap.warwick.ac.uk/id/eprint/77654/> to produce all results.

S1 The stochastic simulation algorithm (SSA)

Consider paths of $\{\mathbf{Y}(t) \mid t \geq 0\}$ whose time-evolution is given by the random time change representation (RTC),

$$\mathbf{Y}(t) = \mathbf{Y}(0) + \sum_{j=1}^r \nu_j N_j \left(\int_0^t \pi_j(\mathbf{Y}(s)) ds \right), \quad (18)$$

where, for $j \in \{1, \dots, r\}$, N_j are independent, unit Poisson processes corresponding to reaction R_j . To simulate such paths, the stochastic simulation algorithm (SSA) generates the next reaction at any given state. That is, if $\hat{\tau} > 0$ and $k \in \{1, 2, \dots, r\}$ correspond to the time to the next reaction and the index of the next reaction, respectively, it can be shown that, given the current state at time $t \geq 0$, $\mathbf{Y}(t) = \mathbf{y}$, the joint probability density function $p(\hat{\tau}, k \mid \mathbf{y}, t)$ of $\hat{\tau}$ and k are

$$p(\hat{\tau}, k \mid \mathbf{y}, t) = \pi_k(\mathbf{y}) \exp \left(- \sum_{j=1}^r \pi_j(\mathbf{y}) \tau \right). \quad (19)$$

where π_k the propensity function of reaction k . Informally, $p(\hat{\tau}, k \mid \mathbf{y}, t) d\tau$ represents the probability that, given that $\mathbf{Y}(t) = \mathbf{y}$, the next reaction in the system will occur at in the infinitesimal time interval $[t + \hat{\tau}, t + \hat{\tau} + d\hat{\tau})$ and will be a R_k reaction. Equation (19) implies that $\hat{\tau}$ is an exponential random variable with mean $1 / \sum_{j=1}^r \pi_j(\mathbf{y})$ and k is a statistically independent to τ integer random variable with point probabilities $\pi_k(\mathbf{y}) / \sum_{j=1}^r \pi_j(\mathbf{y})$. Hence we can sample such random variables exactly using the following; generate two random numbers, r_1 and r_2 , from the uniform distribution in the unit interval and take,

$$\hat{\tau} = - \frac{\log(r_1)}{\sum_{j=1}^r \pi_j(\mathbf{y})}, \quad (20)$$

and k to be the smallest integer with $k \leq r$ such that,

$$\sum_{j=1}^k \pi_j(\mathbf{y}) > r_2 \sum_{j=1}^r \pi_j(\mathbf{y}). \quad (21)$$

Using the sampling procedure given by (20) and (21), we are able to construct the SSA for paths of $\{\mathbf{Y}(t) \mid t \geq 0\}$ which evolve exactly according to (18). This is given in Algorithm 5.

Here the output sequence (t_j, \mathbf{y}_j) , $j = 1, 2, \dots$, fully describes the evolution of a stochastic trajectory $\{\mathbf{Y}(t) : 0 \leq t \leq T\}$. Note that $\mathbf{Y}(t) = \mathbf{y}(t_j)$ for $t_j \leq t < t_{j+1}$. These paths are exact consequences of the chemical physics of stochastic reaction networks and hence capture the true dynamics of the network. For further details see [13, 14]. Consequently, one can compare distributions of states simulated by a model to that by the SSA in order to test the statistical accuracy of the model.

Algorithm 5 Stochastic Simulation Algorithm (SSA)

Inputs: Initial conditions: $t_0 = 0$, $\mathbf{Y}(0) = \mathbf{y}_0$, $i = 0$. Parameter $T > 0$.

Steps: While $t < T$

1. generate two random numbers, r_1 and r_2 , from the uniform distribution on the unit interval;
2. sample $\hat{\tau}$ according to (20) and k according to (21);
3. update $t \leftarrow t + \hat{\tau}$ and $\mathbf{y} \leftarrow \mathbf{y} + \boldsymbol{\nu}_k$;
4. update $i \leftarrow i + 1$ and store t in t_i and \mathbf{y} in \mathbf{y}_i .

Outputs: (t_j, \mathbf{y}_j) , $j = 1, \dots, i$

Algorithm 6 SSA with thinning

Inputs: Initial conditions: $t_0 = 0$, $\mathbf{Y}(0) = \mathbf{y}_0$, $i = 0$, $m = 1$. Parameter $T > 0$, $\delta t > 0$, M positive integer.

Steps: While $t < T$ and $m \leq M$

1. generate two random numbers, r_1 and r_2 , from the uniform distribution on the unit interval;
2. sample $\hat{\tau}$ according to (20) and k according to (21);
3. update $t \leftarrow t + \hat{\tau}$ and $\mathbf{y} \leftarrow \mathbf{y} + \boldsymbol{\nu}_k$;
4. update $i \leftarrow i + 1$ and
 - if $t \in (m\delta t, (m+1)\delta t)$, then store t in t_m and \mathbf{y} in \mathbf{y}_m , and update $m \leftarrow m + 1$,
 - if $t > (m+1)\delta t$, end procedure with message “increase δt and run again.”.

Outputs: (t_j, \mathbf{y}_j) , $j = 1, \dots, m$

When performing the SSA simulations, we used the so-called *thinning* method to reduce the computational memory used. That is, we used the Algorithm 6. This records the SSA generated states at the first reaction times after times $m\delta t$, $m = 0, 1, 2, \dots, M$, for some large M and fairly small δt . Furthermore, when we wish to compare SSA with pcLNA at specific times we use a smoothing spline interpolation to get the state of SSA (and similarly pcLNA) at specific time, say $t \in [(m-1)\delta t, m\delta t]$.

S2 The derivation of the Linear Noise Approximation (LNA)

To simplify notation, in this section we use the notation $x_t = x(t)$, for all states considered (i.e. \mathbf{x} , $\boldsymbol{\xi}$, \mathbf{X}). The LNA ansatz,

$$\mathbf{X}(t) = \mathbf{x}(t) + \Omega^{-1/2}\boldsymbol{\xi}(t),$$

implies that

$$\boldsymbol{\xi}_t = \sqrt{\Omega}(\mathbf{X}_t - \mathbf{x}_t)$$

and thus

$$\boldsymbol{\xi}_{t+dt} - \boldsymbol{\xi}_t = \sqrt{\Omega}((\mathbf{X}_{t+dt} - \mathbf{X}_t) - (\mathbf{x}_{t+dt} - \mathbf{x}_t)).$$

Using the form of RTC for \mathbf{X} and the RRE, we get that

$$\boldsymbol{\xi}_{t+dt} - \boldsymbol{\xi}_t = \sqrt{\Omega} \left(\sum_{j=1}^r \boldsymbol{\nu}_j \{ \Omega^{-1} N_j (\Omega \rho_j(\mathbf{X}_t) dt) - \rho_j(\mathbf{x}_t) dt \} \right).$$

We next insert in the above sum the zero terms $0 = \rho_j(\mathbf{X}_t) dt - \rho_j(\mathbf{x}_t) dt$, where $\rho_j(\mathbf{X}_t) dt$ the mean of $\Omega^{-1} N_j (\Omega \rho_j(\mathbf{X}_t) dt)$, to get

$$\boldsymbol{\xi}_{t+dt} - \boldsymbol{\xi}_t = \sqrt{\Omega} \left(\sum_{j=1}^r \boldsymbol{\nu}_j \{ \Omega^{-1} N_j (\Omega \rho_j(\mathbf{X}_t) dt) - \rho_j(\mathbf{X}_t) dt + (\rho_j(\mathbf{X}_t) - \rho_j(\mathbf{x}_t)) dt \} \right).$$

Then, by the Central Limit Theorem, as $\Omega \rightarrow \infty$,

$$Z = \frac{\Omega^{-1} N_j (\Omega \rho_j(\mathbf{X}_t) dt) - \rho_j(\mathbf{X}_t) dt}{\sqrt{\Omega^{-1} \rho_j(\mathbf{X}_t) dt}} \sim N(0, 1)$$

where $N(0, 1)$ is the standard normal distribution. Then for sufficiently large Ω ,

$$\sqrt{\Omega} (\Omega^{-1} N_j (\Omega \rho_j(\mathbf{X}_t) dt) - \rho_j(\mathbf{X}_t) dt) \approx Z \sqrt{\rho_j(\mathbf{x}_t) dt}. \quad (22)$$

Furthermore, by applying a Taylor expansion of $\rho_j(\mathbf{X}_t)$ about \mathbf{x}_t , we get

$$\sqrt{\Omega} (\rho_j(\mathbf{X}_t) - \rho_j(\mathbf{x}_t)) = \boldsymbol{\xi}(t)^T \nabla_{\mathbf{x}} \rho_j(\mathbf{x}_t) + O(\Omega^{-1/2}), \quad (23)$$

where $\nabla_{\mathbf{x}}^T = (\partial/\partial x_1, \dots, \partial/\partial x_n)$. Hence, for sufficiently large Ω ,

$$\boldsymbol{\xi}_{t+dt} - \boldsymbol{\xi}_t \approx \sum_j \boldsymbol{\nu}_j \boldsymbol{\xi}(t)^T \nabla_{\mathbf{x}} \rho_j(\mathbf{x}_t) dt + \sum_j Z_j \boldsymbol{\nu}_j \sqrt{\rho_j(\mathbf{x}_t) dt}$$

where Z_j are independent random variables following the standard normal distribution. Writing the above equation in matrix form, we get

$$d\boldsymbol{\xi} = \mathbf{J}\boldsymbol{\xi} dt + \mathbf{E} d\mathbf{B}_t, \quad (24)$$

where \mathbf{J} is the Jacobian matrix of the RRE, $\mathbf{E} = \mathbf{E}(\mathbf{x}) = \mathbf{S} \text{diag}(\sqrt{\rho_1(\mathbf{x})}, \dots, \sqrt{\rho_r(\mathbf{x})})$ the product of the stoichiometry matrix $\mathbf{S} = [\boldsymbol{\nu}_1 \cdots \boldsymbol{\nu}_r]$, and the square root of the diagonal matrix, with main diagonal entries $(\rho_1(\mathbf{x}), \dots, \rho_r(\mathbf{x}))$, and \mathbf{B}_t an n -dimensional Wiener process.

S3 Centre manifold theory

Different dynamical systems can be grouped together based on the qualitative similarity of their behavior near their equilibrium points.

Definition 1 (Topological equivalence). *Consider two ODE systems as in 6 with velocities, \mathbf{F} and \mathbf{F}' , on \mathbb{R}^n and \mathbb{R}^m respectively. Suppose they each have an equilibrium point, \mathbf{x}_0 and \mathbf{x}'_0 , respectively. Then, near their equilibrium, the two dynamical systems are locally topologically equivalent if there exists a homeomorphism $\mathbf{h} : \mathbb{R}^n \rightarrow \mathbb{R}^m$ that is,*

- (i) defined in a neighbourhood $A \subset \mathbb{R}^n$ of \mathbf{x}_0 ;
- (ii) satisfies $\mathbf{x}'_0 = \mathbf{h}(\mathbf{x}_0)$;
- (iii) maps paths of the system with velocity \mathbf{F} in the neighbourhood A onto paths of the system with velocity \mathbf{F}' in the neighbourhood $\mathbf{h}(A) \subset \mathbb{R}^m$, preserving the direction of time.

Intuitively, this means the paths of one dynamical system near its equilibrium can be continuously deformed onto paths of the other dynamical system near its equilibrium, and hence both systems exhibit paths that are qualitatively similar, i.e. have the same key features, near their equilibria.

The deterministic evolution $\{\mathbf{x}(t) \mid t \geq 0\}$ solving the reaction rate equation (RRE) (6) when one parameter, say $\alpha \in \mathbb{R}$, is free to vary. We assume that the system has a non-hyperbolic equilibrium. That is, there exists an $\alpha_p \in \mathbb{R}$ such that,

$$\mathbf{F}(\mathbf{x}_{\alpha_p}, \alpha_p) = \mathbf{0} \quad \text{and} \quad n_0 > 0, \quad (25)$$

where n_0, n_+, n_- denote the number of eigenvalues of the Jacobian matrix $\mathbf{J}(\mathbf{x}_{\alpha_p}, \alpha_p)$ with zero, positive and negative real part, respectively. Following this, consider the extended system,

$$\begin{cases} \dot{\mathbf{x}} = \mathbf{F}(\mathbf{x}, \alpha), \\ \dot{\alpha} = 0. \end{cases} \quad (26)$$

Note that the Jacobian matrix of (26) evaluated at $\mathbf{x} = \mathbf{x}_{\alpha_p}$ and $\alpha = \alpha_p$ is the $(n+1) \times (n+1)$ matrix,

$$\begin{pmatrix} 0 & 0 \\ \frac{\partial \mathbf{F}}{\partial \alpha} \Big|_{\substack{\mathbf{x}=\mathbf{x}_{\alpha_p} \\ \alpha=\alpha_p}} & \mathbf{J}(\mathbf{x}_{\alpha_p}, \alpha_p) \end{pmatrix}, \quad (27)$$

with $n_0 + 1$ eigenvalues with zero real part and $n - n_0$ eigenvalues with nonzero real part. Under the assumptions above, the following theorem holds (see [34, Theorem 5.1 and Lemma 5.1]).

Theorem 1 (Center Manifold Theorem). *Let T^c be the eigenspace corresponding to the $n_0 + 1$ eigenvalues of (27) with zero real part. Then, there exists a smooth $(n_0 + 1)$ -dimensional manifold \mathcal{W}^c defined locally to $\mathbf{x} = \mathbf{x}_{\alpha_p}$ and $\alpha = \alpha_p$ and tangent to T^c at $\mathbf{x} = \mathbf{x}_{\alpha_p}$ and $\alpha = \alpha_p$. Moreover since $\dot{\alpha} = 0$ the hyperplanes, $\Pi_{\alpha'} = \{(\mathbf{x}, \alpha) \mid \alpha = \alpha'\}$, $\alpha' \in \mathbb{R}$ are invariant with respect to (26) and so, for each α local to α_p , \mathcal{W}^c is foliated by the n_0 dimensional manifolds $\mathcal{W}_\alpha^c = \mathcal{W}^c \cap \Pi_\alpha$. For each α local to α_p we call \mathcal{W}_α^c the centre manifold. Finally, for each α local to α_p , there exists a neighbourhood $\Delta(\mathbf{x}_{\alpha_p})$ of $\mathbf{x} = \mathbf{x}_{\alpha_p}$ such that if a path of (6) starting in $\Delta(\mathbf{x}_{\alpha_p})$, remains in $\Delta(\mathbf{x}_{\alpha_p})$, then this path approach \mathcal{W}_α^c as $t \rightarrow \infty$.*

In other words, the Center Manifold Theorem states that there exists a parameter-dependent n_0 -dimensional invariant center manifold \mathcal{W}_α^c which is locally attracting. The next theorem (see [52]) describes a decomposition of non-hyperbolic systems into a linear and a non-linear component.

Theorem 2 (Shoshitaishvili Reduction Principle). *Let α be local to α_p and let $(\mathbf{u}, \mathbf{v}, \mathbf{w})$ be a coordinate system with coordinates, $\mathbf{u} \in \mathbb{R}^{n_0}$, $\mathbf{v} \in \mathbb{R}^{n_+}$ and $\mathbf{w} \in \mathbb{R}^{n_-}$ lying on the eigenspaces corresponding to the n_0, n_+, n_- eigenvalues of $\mathbf{J}(\mathbf{x}_\alpha, \alpha)$ with zero, positive and negative real part, when $\alpha = \alpha_p$, respectively.*

Then, the centre manifold \mathcal{W}_α^c can be locally represented as a graph of a smooth function $\mathbf{V}_\alpha : \mathbb{R}^{n_0} \rightarrow \mathbb{R}^{n_+ + n_-}$ with $\mathbf{V}_\alpha(\mathbf{u}) = O(\|\mathbf{u}\|^2)^3$;

$$\mathcal{W}_\alpha^c = \{(\mathbf{u}, \mathbf{v}, \mathbf{w}) \mid (\mathbf{v}, \mathbf{w}) = \mathbf{V}_\alpha(\mathbf{u})\}.$$

³This implies that the Taylor expansion of $\mathbf{V}_\alpha(\mathbf{u})$ starts with at least quadratic terms.

Moreover, near the equilibrium \mathbf{x}_p , (6) is locally topologically equivalent to the following system;

$$\begin{cases} \dot{\mathbf{u}} = \mathbf{A}\mathbf{u} + \mathbf{g}(\mathbf{u}, \mathbf{V}_\alpha(\mathbf{u})), \\ \dot{\mathbf{v}} = -\mathbf{v}, \\ \dot{\mathbf{w}} = \mathbf{w}, \end{cases} \quad (28)$$

near its equilibrium. Here \mathbf{A} is an $n_0 \times n_0$ matrix with all its eigenvalues, for $\alpha = \alpha_p$, on the imaginary axis and $\mathbf{g} : \mathbb{R}^n \rightarrow \mathbb{R}^{n_0}$ is a smooth function with Taylor expansions starting with at least quadratic terms.

The first equation in (28) is a restriction of equation (26) on the center manifold \mathcal{W}_α^c . The other two equations in (28) present linear, transient dynamics. Therefore, for small $|\alpha - \alpha_p|$, all non-transient events are captured on the invariant \mathcal{W}_α^c by the n_0 -dimensional system of \mathbf{u} , where n_0 can be much smaller than n . It is worth noting that if $n_+ = 0$, the third equation vanishes, and the center manifold \mathcal{W}_α^c is attracting.

S4 Numerical Investigations

S4.1 The NF- κ B reaction network

The NF- κ B network consists of 11 species detailed in Table S1.

Table S1: Details of the 11 species characterising the NF- κ B network and their initial concentrations in three simulation settings with different value of the bifurcation parameter.

	Name	Description	Initial values Fig. S9	Initial values Fig. S10	Initial values Fig. S11
1	N_c	Free Cytoplasmic NF κ B	0.0059	0.0065	0.0044
2	I_c	Free Cytoplasmic I κ Ba	0.0119	0.0289	0.0267
3	NI_c	Cytoplasmic NF κ B-I κ Ba	0.0096	0.0611	0.0442
4	N_n	Free nuclear NF κ B	0.0639	0.0111	0.0305
5	I_n	Free nuclear I κ Ba	0.0001	0.0010	0.0003
6	NI_n	Nuclear NF κ B-I κ Ba	0.0002	0.0005	0.0005
7	I_m	I κ Ba transcription	0.0001	0.0002	0.0002
8	K_n	Kinase IKK η	0.0368	0.0071	0.0015
9	K_a	Kinase IKK α	0.0083	0.0034	0.0023
10	A_m	A20 transcription	0.0001	0.0001	0.0001
11	A	A20	0.0117	0.0139	0.0135

Table S2: The parameters of NF- κ B system and the values used in simulations. Each of the three different levels of TNF α displayed in last row are used for the simulations in Figures S9,S10,S11, respectively.

parameter	description	value	unit
k_v	Cytoplasm:Nucleus ratio	3.3	–
k_p	IKKn production	0.0006	s^{-1}
k_a	Activation caused by TNF α	0.004	s^{-1}
k_i	Spontaneous IKK activation	0.003	s^{-1}
k_{a1a}	NFkB-IkBa association	0.5	$\mu M^{-1} s^{-1}$
k_{d1a}	NFkB-IkBa dissociation	0.0005	s^{-1}
k_{c1a}	Catalysis of IKK-IkBa dimer	0.074	s^{-1}
k_{c2a}	Catalysis of IKK-IkBa-NFkB trimer	0.37	s^{-1}
k_{t2a}	degradation of IkBa (IKK dependent from trimer)	0.1	s^{-1}
c_{4a}	Free IkBa degradation	0.0005	s^{-1}
c_{5a}	NFkB complexed IkBa degradation	0.000022	s^{-1}
k_{i1}	NFkB nuclear import	0.0026	s^{-1}
k_{e1}	NFkB nuclear export	0.000052	s^{-1}
k_{e2a}	NFkB-IkBa nuclear export	0.01	s^{-1}
k_{i3a}	IkBa nuclear import	0.00067	s^{-1}
k_{e3a}	IkBa nuclear export	0.000335	s^{-1}
h	Order of hill function	2	–
k	Hill constant	0.0650	$\mu M/L$
c_{1a}	IkBa mRNA synthesis	1.400e-07	$\mu M^{-1} s^{-1}$
c_{2a}	IkBa translation rate	0.5	s^{-1}
c_{3a}	IkBa mRNA degradation	0.0003	s^{-1}
c_1	IkBa mRNA synthesis	1.4e-07	$\mu M^{-1} s^{-1}$
c_2	A20 mRNA translation	0.5	s^{-1}
c_3	A20 mRNA degradation	0.00048	s^{-1}
c_4	A20 degradation	0.0045	s^{-1}
$k_{b,A20}$	Half-max A20 inhibition concentration	0.0018	$\mu M/L$
TNF- κ B	total NF- κ B concentration	0.08	μM
TIKK	total IKK concentration	0.08	μM
TNF α	Tumor necrosis factor alpha level	1.5 / 3.66 / 10	ng/mL

The ODE system for the NF- κ B system are given in table

Table S3: The RRE ODE system equations for the NF- κ B system in [4]

\dot{N}_c	$= k_{d1a}NI_c - k_{a1a}N_cI_c - k_{i1}N_c + c_{5a}NI_c + k_vk_{e1}N_n + k_{t2a} \times (TNFKB - N_c - NI_c - N_n + NI_n)$
\dot{I}_c	$= k_{d1a}NI_c - k_{a1a}N_cI_c - k_{i3a}I_c + k_vk_{e3a}I_n - c_{4a}I_c + c_{2a}I_m - k_{c1a}K_aI_c$
\dot{NI}_c	$= k_{a1a}N_cI_c - k_{d1a}NI_c + k_vk_{e2a}NI_n - c_{5a}NI_c - k_{c2a}K_aNI_c$
\dot{N}_n	$= k_{d1a}NI_n - k_vk_{a1a}N_nI_n + k_{i1}N_c - k_vk_{e1}N_n$
\dot{I}_n	$= k_{d1a}NI_n - k_vk_{a1a}N_nI_n + k_{i3a}I_c - k_vk_{e3a}I_n - c_{4a}I_n$
\dot{NI}_n	$= k_vk_{a1a}NI_n - k_{d1a}NI_n - k_vk_{e2a}NI_n$
\dot{I}_m	$= c_{1a}(N_n^h/(N_n^h + (k/k_v)^h)) - c_{3a}I_m$
\dot{K}_n	$= k_p(TIKK - K_n - K_a)(k_{bA20}/(k_{bA20} + A \times TNF\alpha/10)) - k_aTNF\alpha K_n/10$
\dot{K}_a	$= k_aTNF\alpha K_n/10 - k_iK_a$
\dot{A}_m	$= c_1(N_n^h/(N_n^h + (k/k_v)^h)) - c_3A_m$
\dot{A}	$= c_2A_m - c_4A$

The reaction rates used for the SSA are provided in the table below. The values of the parameters are the same as in Table S2 with suitable rate constant conversions applied.

Table S4: The reactions and the corresponding propensity functions used for the SSA simulations of the NF- κ B system.

reaction	rate
$N_c + I_c \xrightarrow{k_{a1a}} NI_c$	$k_{a1a} \times I_c \times N_c / \Omega$
$NI_c \xrightarrow{k_{d1a}} N_c + I_c$	$k_{d1a} \times NI_c$
$N_n + I_n \xrightarrow{k_{a1a}} NI_n$	$k_v k_{a1a} \times I_n \times N_n / \Omega$
$NI_n \xrightarrow{k_{d1a}} N_n + I_n$	$k_{d1an} \times NI_n$
$K_a + I_c \xrightarrow{k_{c1a}} K_a + I_p$	$k_{c1a} \times K_a \times I_c / \Omega$
$K_a + NI_c \xrightarrow{k_{c2a}} K_a + NI_p$	$k_{c2a} \times K_a \times NI_c / \Omega$
$NI_p \xrightarrow{k_{t2a}} N_c$	$k_{t2a} \times NI_p$
$N_c \xrightarrow{k_{i1}} N_n$	$k_{i1} \times N_c$
$N_n \xrightarrow{k_{e1}} N_c$	$k_{e1} \times k_v \times N_n$
$NI_n \xrightarrow{k_{e2a}} NI_c$	$k_{e2a} \times k_v \times NI_n$
$I_c \xrightarrow{k_{i3a}} I_n$	$k_{i3a} \times I_c$
$I_n \xrightarrow{k_{e3a}} I_c$	$k_{e3a} \times k_v \times I_c$
$\emptyset \xrightarrow{H_I} I_m$	$(c_{1a}\Omega) \frac{N_n^h}{N_n^h + (k\Omega/k_v)^h}$
$I_m \xrightarrow{c_{2a}} I_m + I_c$	$c_{2a} \times I_m$
$I_m \xrightarrow{c_{3a}} \emptyset$	$c_{3a} \times I_m$
$I_c \xrightarrow{c_{4a}} \emptyset$	$c_{4a} \times I_c$
$I_n \xrightarrow{c_{4a}} \emptyset$	$c_{4a} \times I_n$
$NI_c \xrightarrow{c_{5a}} N_c$	$c_{5a} \times NI_c$
$\emptyset \xrightarrow{H_A} A_m$	$(c_1\Omega) \frac{N_n^h}{N_n^h + (k\Omega/k_v)^h}$
$A_m \xrightarrow{c_2} A_m + A$	$c_2 \times A_m$
$A_m \xrightarrow{c_3} \emptyset$	$c_3 \times A_m$
$A \xrightarrow{c_4} \emptyset$	$c_4 \times A$
$K_i \xrightarrow{M_A} K_n$	$k_p(TIKK - K_n - K_a) \frac{k_{b,A20} \times \Omega}{(k_{b,A20}\Omega) + A \times TNF\alpha / 10}$
$K_n \xrightarrow{TNF\alpha / 10 \times k_a} K_a$	$TNF\alpha / 10 \times k_a \times K_n$
$K_a \xrightarrow{k_i} K_i$	$k_i \times K_a$

S4.1.1 Details for Figure 3A

The bifurcation parameter of this system is the level of the Tumor necrosis factor alpha level (TNF α). The Hopf bifurcation value is $\approx 3.66ng/mL$. The simulations in Figure 3A are produced with the level of TNF α at the Hopf bifurcation value and with initial conditions given in Table S1 in the column “Initial values Fig. S10”.

The empirical density functions of the probability distribution of each variable are derived using the kernel density function “ksdensity” in MATLAB [25]. To ensure good visibility of all the curves, we scale them. Specifically, both the x - and z -axis range from 0 to 1 since we divide both the value of each variable and their densities obtained for both SSA and pcLNA by their maximum observed values for both algorithms.

S4.1.2 Further numerical investigations for the NF- κ B system

See Figures S9, S10, S11.

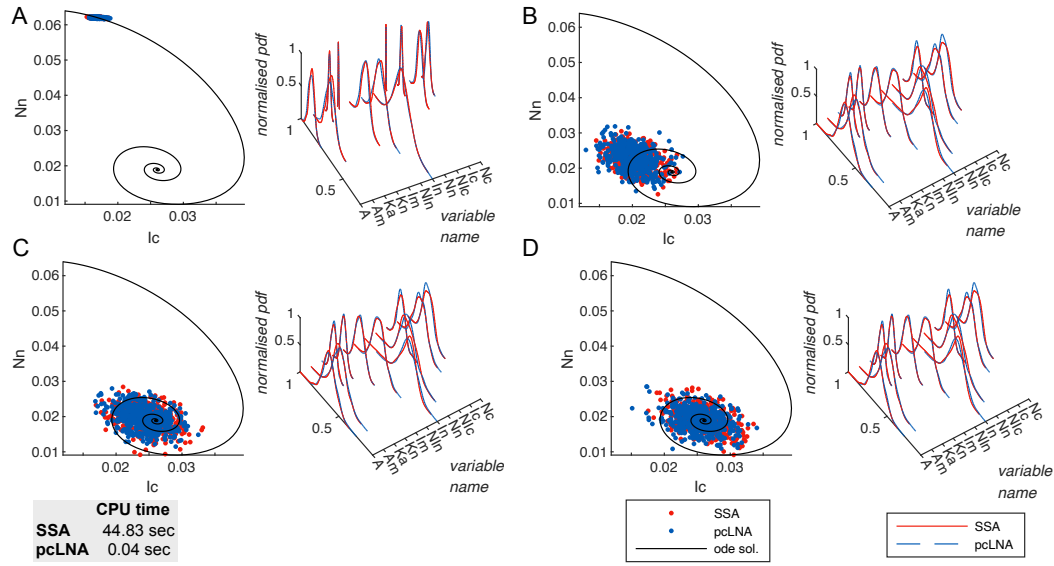


Figure S9: Comparison between SSA (red) and pcLNA (blue) for the NF- κ B system at $\Omega = 600,000$ with $\text{TNF}\alpha$ level = 1.5 ng/mL. Panels (A)–(D) correspond to times $t = 5, \tau + 5, 2\tau + 5, 3\tau + 5$, where $\tau \approx 102.095$ is the oscillation period. Each panel shows (left) the states recorded at time t of the simulations with solutions of the corresponding RRE, and (right) the corresponding empirical probability density functions of each system variable. Initial conditions and parameter values are given in Tables S1 and S2.

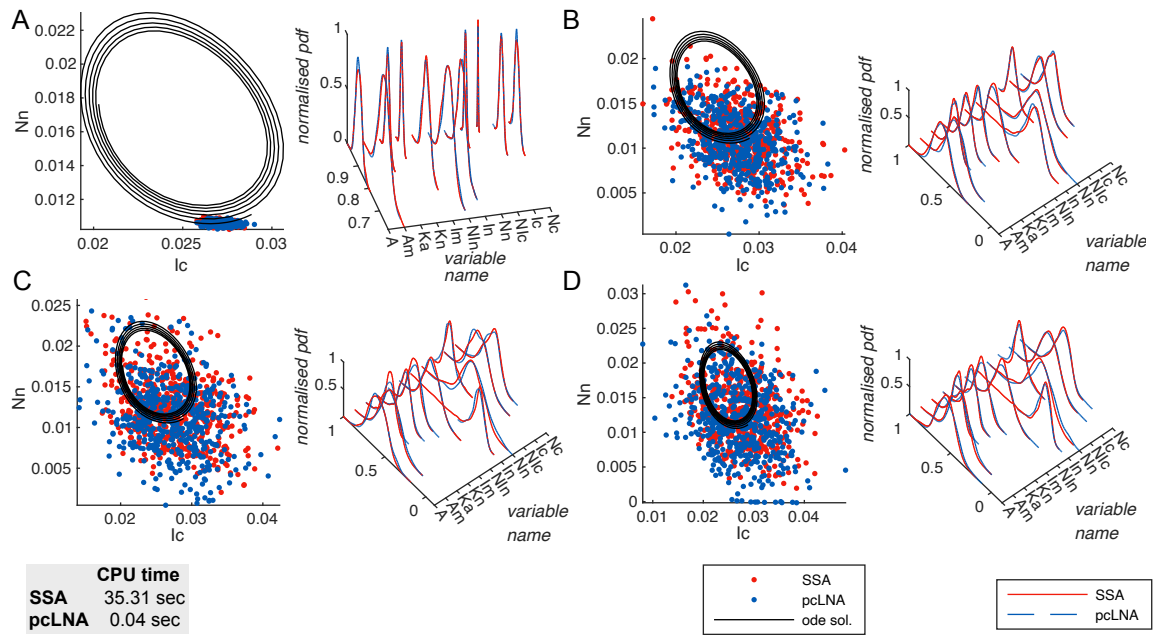


Figure S10: Comparison between SSA (red) and pcLNA (blue) for the NF- κ B system at $\Omega = 600,000$ with TNF α level = 3.66 ng/mL (Hopf bifurcation point). Panels (A)–(D) correspond to times $t = 5, \tau + 5, 2\tau + 5, 3\tau + 5$, where $\tau \approx 102.095$ is the oscillation period. Each panel shows (left) the states recorded at time t of the simulations with solutions of the corresponding RRE, and (right) the corresponding empirical probability density functions of each system variable. Initial conditions and parameter values are provided in Tables S1 and S2.

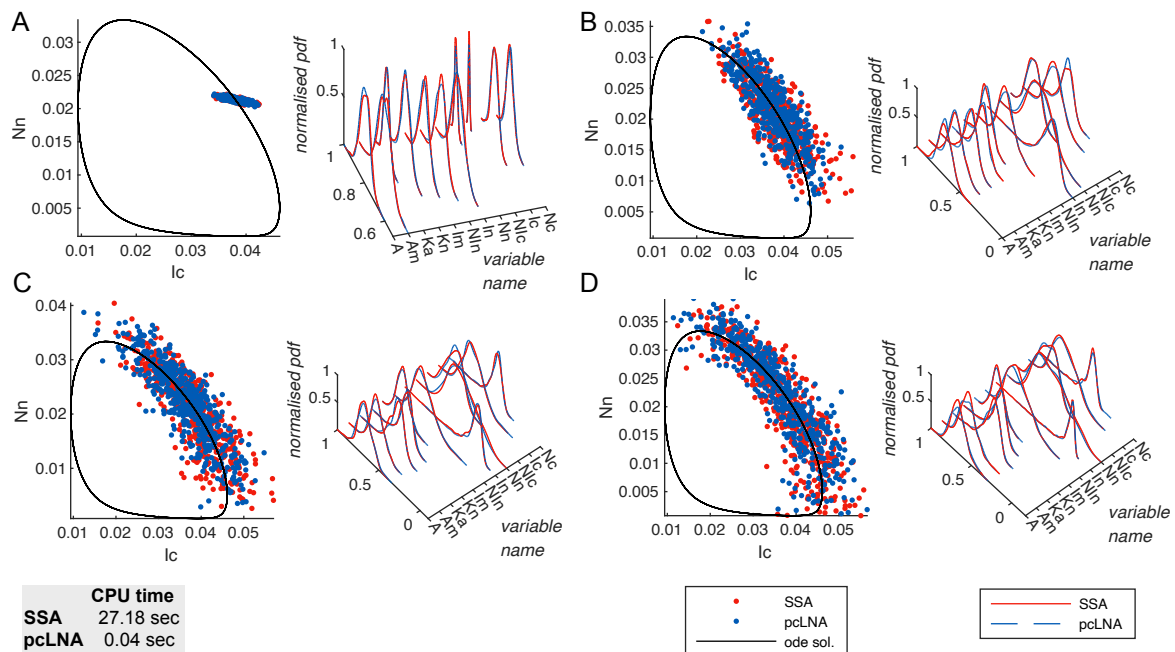
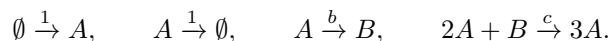


Figure S11: Comparison between SSA (red) and pcLNA (blue) for the NF- κ B system at $\Omega = 600,000$ with TNF α level = 10 ng/mL. Panels (A)–(D) correspond to times $t = 5, \tau + 5, 2\tau + 5, 3\tau + 5$, where $\tau \approx 102.095$ is the oscillation period. Each panel shows (left) the states recorded at time t of the simulations with solutions of the corresponding RRE, and (right) the corresponding empirical probability density functions of each system variable. Initial conditions and parameter values are listed in Tables S1 and S2.

S4.2 The Brusselator reaction network

The two dimensional Brusselator network, introduced in [35], consists of two chemical species, A and B , which undergo the following reactions,



If, for each $t \geq 0$, we let $\mathbf{Y}(t) = (Y_1(t), Y_2(t))^T$ denote the number of molecules of A and B respectively, then these reactions occur according to the following intensities

$$\pi_1 = \Omega, \quad \pi_2 = Y_1, \quad \pi_3 = bY_1, \quad \pi_4 = cY_1^2 Y_2 / \Omega^2.$$

With system size Ω and $\mathbf{X}(t) = \mathbf{Y}(t)/\Omega$ for each $t \geq 0$, the corresponding RRE solution in the $\Omega \rightarrow \infty$ limit is

$$\begin{cases} \dot{x}_1 = 1 - x_1(1 + b - cx_1x_2), \\ \dot{x}_2 = x_1(b - cx_1x_2). \end{cases} \quad (29)$$

From studying the Jacobian matrix of (29), we may conclude the system has a non-hyperbolic equilibrium at $(x_1, x_2) = (1, 2)^T$, when $b = 2$ and $c = 1$, with purely imaginary conjugate eigenvalues $\pm i$. Through small deviations of b we deduce the Hopf bifurcation is supercritical with losses of stability occurring as the eigenvalues cross the imaginary axis. Parameters $b < 2$ give rise to a stable equilibrium, whereas $b > 2$ gives rise to an unstable equilibrium surrounded by a unique and stable limit cycle.

Table S5: Species in the Brusselator network and their initial concentrations for three different values of parameter b .

	Name	Description	Initial values Fig. S12	Initial values Fig. S13	Initial values Fig. S14
1	A	Chemical species A	0.8000	0.8000	1.0340
2	B	Chemical species B	1.5000	1.5000	2.9230

Table S6: Parameters used in the Brusselator network.

Parameter	Description	Value	Unit
c	Catalytic reaction rate	1	$\mu M^{-2} s^{-1}$
b	Conversion rate of A to B	1.7 / 2.0 / 2.3	s^{-1}

Table S7: The RRE ODEs for the mean-field dynamics of the Brusselator in the limit $\Omega \rightarrow \infty$.

$$\begin{aligned} \dot{x}_1 &= 1 - x_1(1 + b - cx_1x_2) \\ \dot{x}_2 &= x_1(b - cx_1x_2) \end{aligned}$$

Table S8: Reactions and their corresponding propensity functions for SSA simulations.

Reaction	Propensity function
$\emptyset \xrightarrow{1} A$	$\pi_1 = \Omega$
$A \xrightarrow{1} \emptyset$	$\pi_2 = Y_1$
$A \xrightarrow{b} B$	$\pi_3 = bY_1$
$2A + B \xrightarrow{c} 3A$	$\pi_4 = cY_1^2Y_2/\Omega^2$

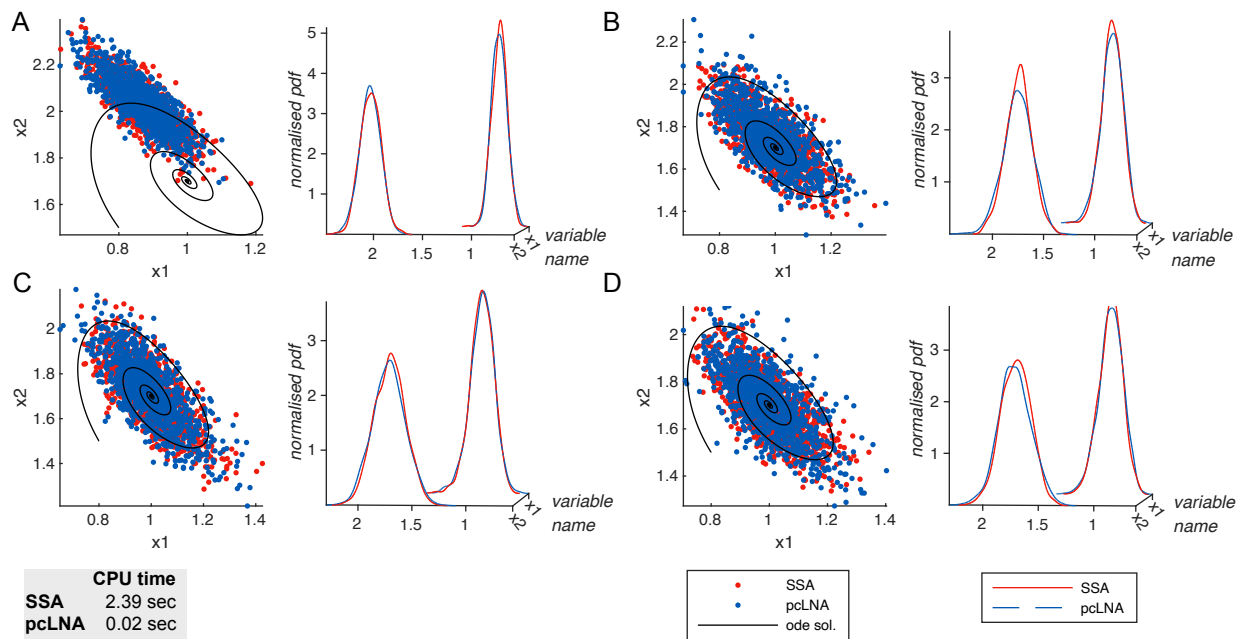


Figure S12: Comparison between SSA (red) and pcLNA (blue) for the Brusselator system at $\Omega = 1000$ with parameter $b = 1.7$. Panels (A)–(D) correspond to times $t = \tau + 0.5$, $3\tau + 0.5$, $5\tau + 0.5$, $7\tau + 0.5$ with period $\tau = 6.2919$. Each panel shows (left) the states recorded at time t of the simulations with solutions of the corresponding RRE, and (right) the corresponding empirical probability density functions of each system variable. Initial conditions and parameter values are given in Tables S5 and S6.

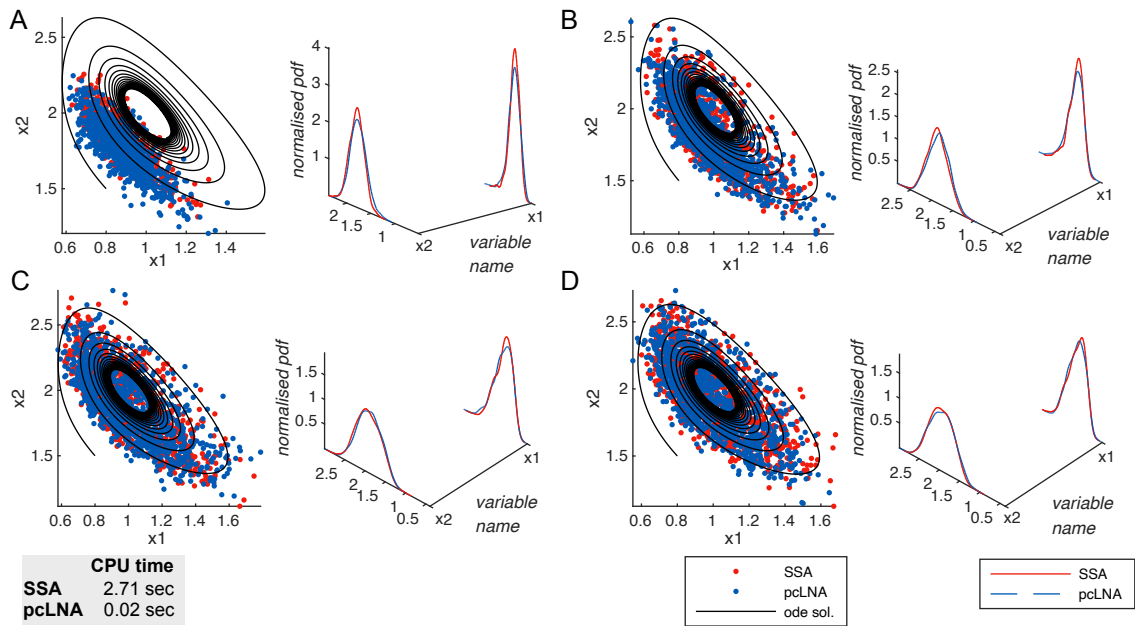


Figure S13: Comparison between SSA (red) and pcLNA (blue) for the Brusselator system at $\Omega = 1000$ with parameter $b = 2$. Panels (A)–(D) correspond to times $t = 0.5, 2\tau + 0.5, 4\tau + 0.5, 6\tau + 0.5$ with period $\tau = 6.35$. Each panel shows (left) the states recorded at time t of the simulations with solutions of the corresponding RRE, and (right) the corresponding empirical probability density functions of each system variable. Initial conditions and parameter values are provided in Tables S5 and S6.

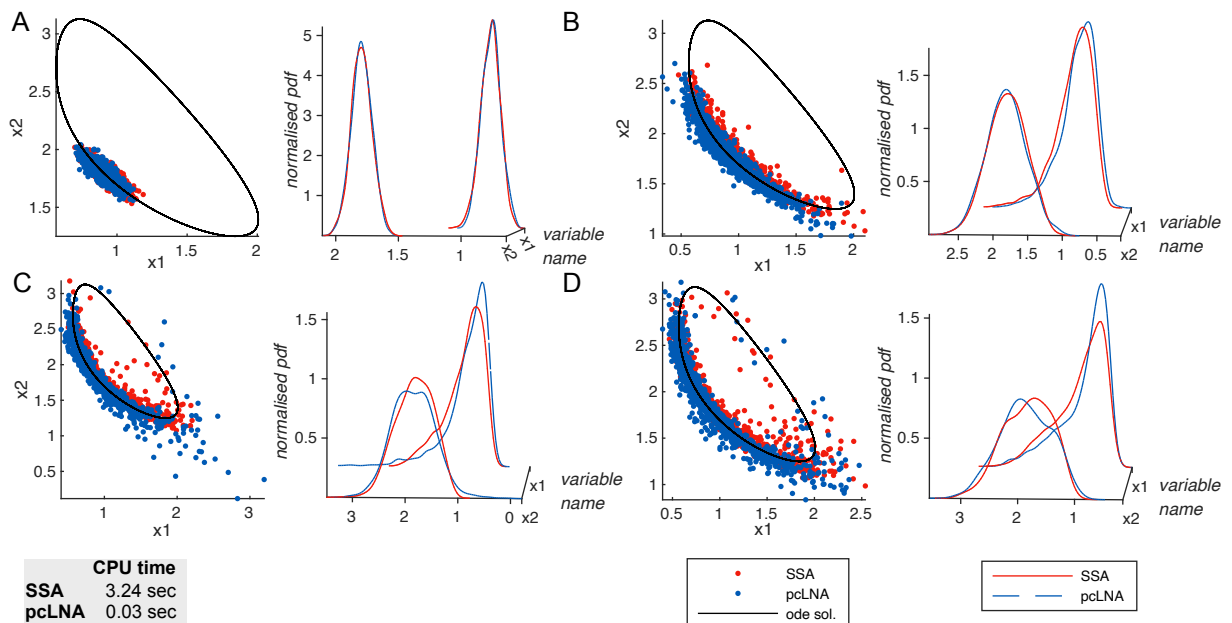


Figure S14: Comparison between SSA (red) and pcLNA (blue) for the Brusselator system at $\Omega = 1000$ with parameter $b = 2.3$. Panels (A)–(D) correspond to times $t = \tau + 0.5$, $3\tau + 0.5$, $5\tau + 0.5$, $7\tau + 0.5$ with period $\tau = 6.4276$. Each panel shows (left) the states recorded at time t of the simulations with solutions of the corresponding RRE, and (right) the corresponding empirical probability density functions of each system variable. Initial conditions and parameter values are listed in Tables S5 and S6.

S4.3 The smallest Hopf bifurcation reaction network

The system is described in [63]. The tables S9, S10, S11, S12 describe the species and their initial conditions, the parameters, the ODE system, and the propensity functions of the SSA simulations of this system, respectively. The results in Figures S15, S16, and S17 are derived using the same method as used for Figure 3 in the main paper. The bifurcation parameter is k_1 and its value at bifurcation is 6.6. The computation of the empirical density functions is done as described in SI section S4.1.1. We used 1000 trajectories of each simulation algorithm to produce the results.

Table S9: Species in the smallest Hopf bifurcation network and their initial concentrations for three different values of parameter k_1 .

	Name	Description	Initial values Fig. S15	Initial values Fig. S16	Initial values Fig. S17
1	X_1	Species 1	3.8220	3.8220	2.4460
2	X_2	Species 2	3.8460	3.8460	1.0720
3	X_3	Species 3	5.1400	5.1400	1.2940

Table S10: Parameters used in the smallest Hopf bifurcation network.

Parameter	Description	Value	Unit
k_1	Activation rate	6 / 6.6 / 7	s^{-1}
k_2	Interaction rate between X_1 and X_2	2.2	s^{-1}
k_3	Degradation rate of X_2	2.2	s^{-1}
k_4	Conversion rate from X_1 to X_3	2.2	s^{-1}
k_5	Conversion rate from X_3 to X_2	2.2	s^{-1}
A	External activation strength	1	–

Table S11: The RRE ODEs for the mean-field dynamics of the smallest Hopf bifurcation network in the limit $\Omega \rightarrow \infty$.

$$\begin{aligned} \dot{x}_1 &= k_1 A x_1 - k_4 x_1 - k_2 x_1 x_2 \\ \dot{x}_2 &= -k_3 x_2 + k_5 x_3 \\ \dot{x}_3 &= k_4 x_1 - k_5 x_3 \end{aligned}$$

Table S12: Reactions and their corresponding propensity functions for SSA simulations.

Reaction	Propensity function
$X_1 \xrightarrow{k_1 A} X_1$	$\pi_1 = k_1 A Y_1$
$X_1 + X_2 \xrightarrow{k_2} \emptyset$	$\pi_2 = k_2 \cdot Y_1 \cdot Y_2 / \Omega$
$X_2 \xrightarrow{k_3} \emptyset$	$\pi_3 = k_3 \cdot Y_2$
$X_1 \xrightarrow{k_4} X_3$	$\pi_4 = k_4 \cdot Y_1$
$X_3 \xrightarrow{k_5} X_2$	$\pi_5 = k_5 \cdot Y_3$

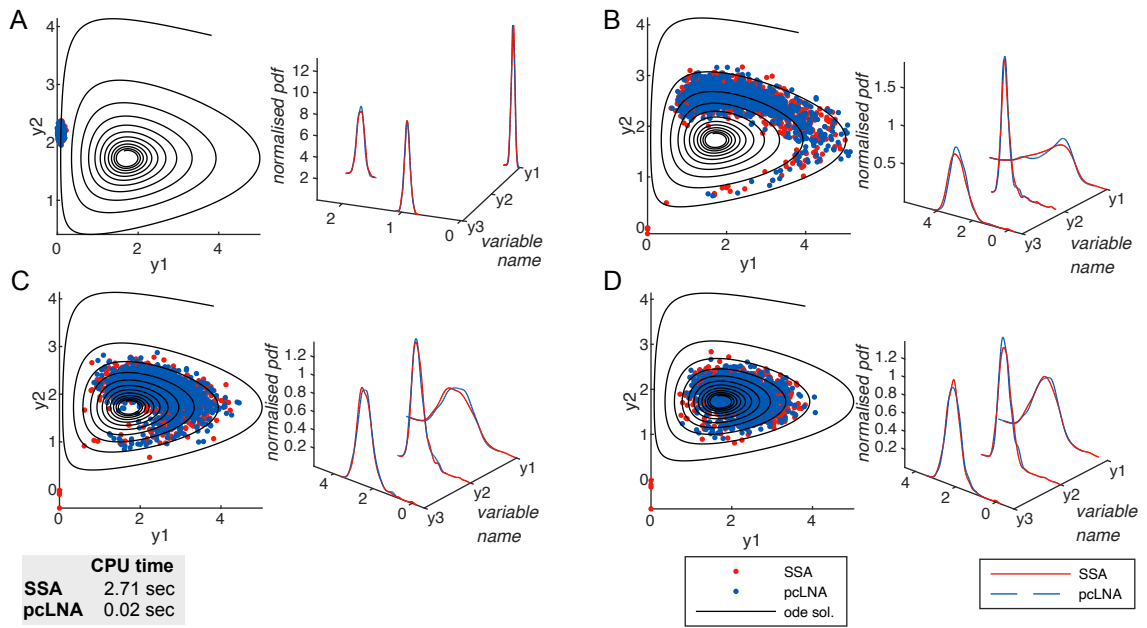


Figure S15: Comparison between SSA (red) and pcLNA (blue) for the smallest Hopf bifurcation network at $\Omega = 500$ with parameter $k_1 = 6$. Panels (A)–(D) correspond to times $t = \tau + 1, 3\tau + 1, 5\tau + 1, 7\tau + 1$ with period $\tau \approx 3$. Each panel shows (left) the states recorded at time t of the simulations with solutions of the corresponding RRE, and (right) the corresponding empirical probability density functions of each system variable. Initial conditions and parameter values are given in Tables S9 and S10.

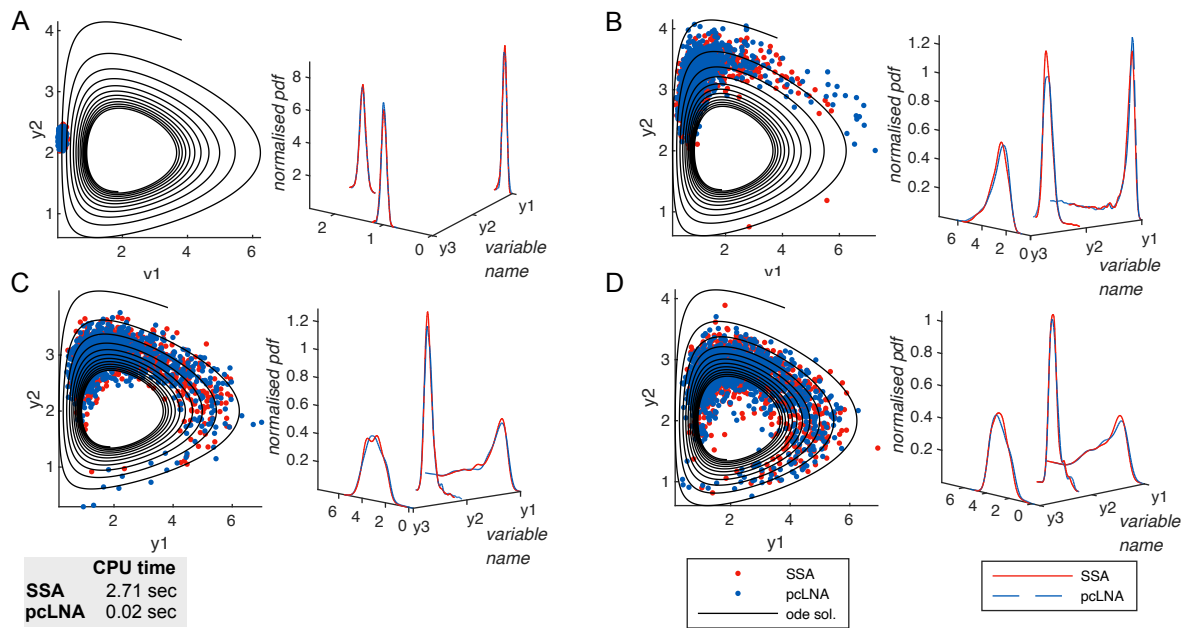


Figure S16: Comparison between SSA (red) and pcLNA (blue) for the smallest Hopf bifurcation network at $\Omega = 500$ with parameter $k_1 = 6.6$. Panels (A)–(D) correspond to times $t = \tau + 1$, $3\tau + 1$, $5\tau + 1$, $7\tau + 1$ with period $\tau \approx 3$. Each panel shows (left) the states recorded at time t of the simulations with solutions of the corresponding RRE, and (right) the corresponding empirical probability density functions of each system variable. Initial conditions and parameter values are provided in Tables S9 and S10.

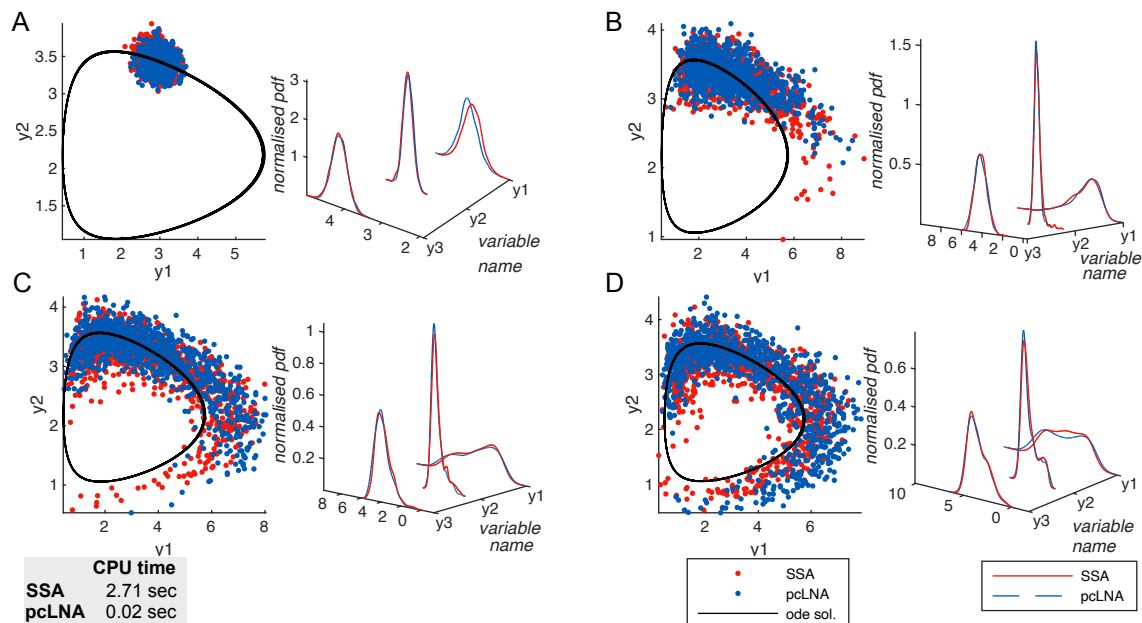


Figure S17: Comparison between SSA (red) and pcLNA (blue) for the smallest Hopf bifurcation network at $\Omega = 500$ with parameter $k_1 = 7$. Panels (A)–(D) correspond to times $t = \tau + 1$, $3\tau + 1$, $5\tau + 1$, $7\tau + 1$ with period $\tau \approx 3$. Each panel shows (left) the states recorded at time t of the simulations with solutions of the corresponding RRE, and (right) the corresponding empirical probability density functions of each system variable. Initial conditions and parameter values are listed in Tables S9 and S10.

S4.4 The Genetic Toggle Switch reaction network

The system is described in [12]. The tables S13, S14, S15, S16 describe the species and their initial conditions, the parameters, the ODE system, and the propensity functions of the SSA simulations of this system, respectively. The results in Figure S18 are derived using the same method as used for Figure 3 in the main paper. The computation of the empirical density functions is done as described in SI section S4.1.1. We used 1000 trajectories of each simulation algorithm to produce the results.

The results in Figure S19 are derived using the same method as used for Figure 3 in the main paper, except for the LNA simulation where the Algorithm is again Algorithm 3 in the main paper except omitting the steps A and C.3 (i.e. no phase correction is applied). The computation of the empirical density functions is done as described in SI section S4.1.1. We used 1000 trajectories of each simulation algorithm to produce the results.

Table S13: Species in the Genetic Toggle Switch network and their initial concentrations.

	Name	Description	Initial values	
			ODE solution 1 Fig. S18	ODE solution 2 Fig. S18
1	x_1	Repressor 1	0.3067	0.4311
2	x_2	Repressor 2	0.4311	0.3067

Table S14: Parameters used in the Genetic Toggle Switch network.

Parameter	Description	Value	Unit
a_1	Activation rate of x_1	1.5	s^{-1}
a_2	Activation rate of x_2	1.5	s^{-1}
b	Hill coefficient for x_2 regulation of x_1	4	–
g	Hill coefficient for x_1 regulation of x_2	4	–
A	External activation strength	1	–

Table S15: The RRE ODEs for the mean-field dynamics of the Genetic Toggle Switch in the limit $\Omega \rightarrow \infty$.

$$\begin{aligned} \dot{x}_1 &= \frac{a_1 A}{1+x_2^b} - x_1 \\ \dot{x}_2 &= \frac{a_2}{1+x_1^g} - x_2 \end{aligned}$$

Table S16: Reactions and their corresponding propensity functions for SSA simulations.

Reaction	Propensity function
$X_1 \xrightarrow{a_1 A} X_1$	$\pi_1 = \frac{a_1 A \cdot \Omega}{1+Y_2^b}$
$X_1 \rightarrow \emptyset$	$\pi_2 = Y_1$
$X_2 \xrightarrow{a_2} X_2$	$\pi_3 = \frac{a_2 \cdot \Omega}{1+Y_1^g}$
$X_2 \rightarrow \emptyset$	$\pi_4 = Y_2$

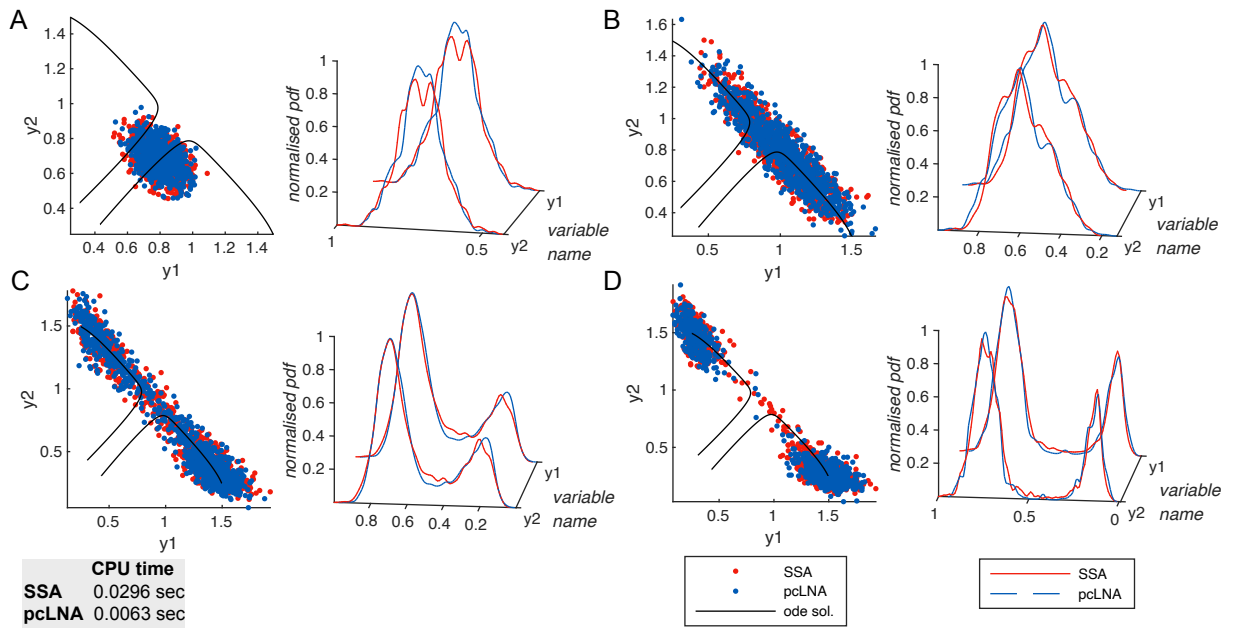


Figure S18: Comparison between SSA (red) and pcLNA (blue) for the Genetic Toggle Switch network at $\Omega = 100$. Panels (A)–(D) correspond to times $t = 0.5006, 2.0024, 5.0059, 9.5051$, respectively. Each panel shows (left) the states recorded at time t of the simulations with solutions of the corresponding RRE, and (right) the corresponding empirical probability density functions of each system variable. The initial conditions for the two ODE solutions are provided in Table S13, and the parameter values are given in Table S14.

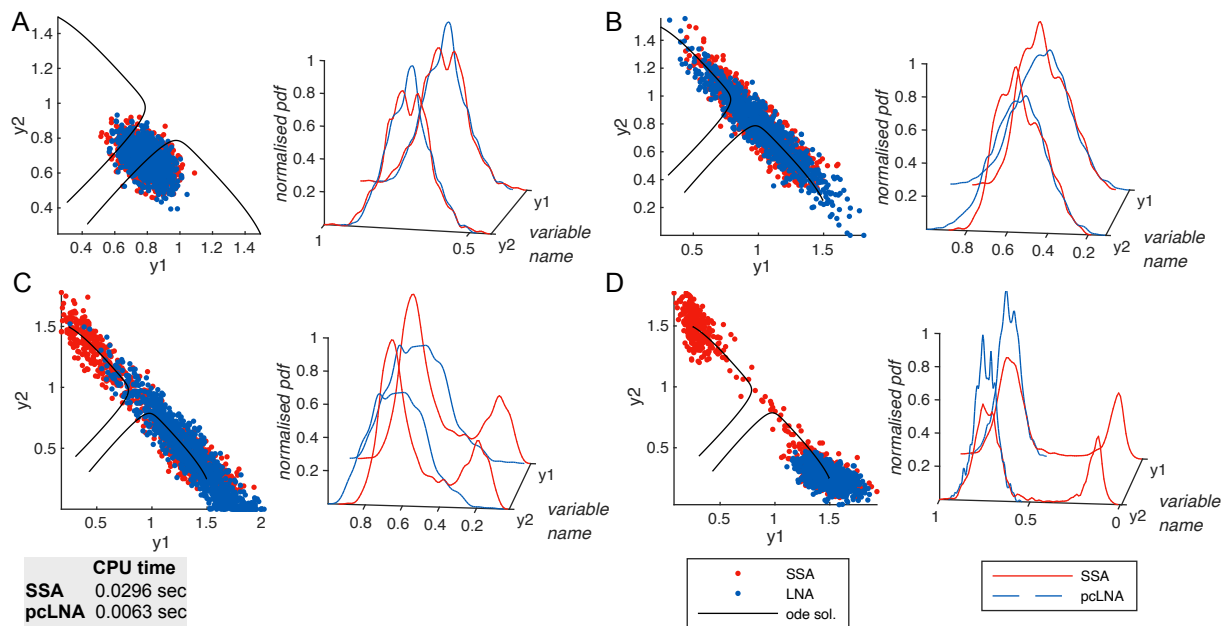


Figure S19: Comparison between SSA (red) and (standard) LNA (blue) for the Genetic Toggle Switch network at $\Omega = 100$. Panels (A)–(D) correspond to times $t = 0.5006, 2.0024, 5.0059, 9.5051$, respectively. Each panel shows (left) the states recorded at time t of the simulations with solutions of the corresponding RRE, and (right) the corresponding empirical probability density functions of each system variable. The initial conditions for the two ODE solutions are provided in Table S13, and the parameter values are given in Table S14.

S4.5 The Cell Cycle reaction network

The system is described in [2]; see section “A Two-Variable Example: The Cdc2-Cyclin B/Wee1 System”. The tables S17, S18, S19, S20 describe the species and their initial conditions, the parameters, the ODE system, and the propensity functions of the SSA simulations of this system, respectively. The results in Figure S20 are derived using the same method as used for Figure 3 in the main paper. The computation of the empirical density functions is done as described in SI section S4.1.1. We used 1000 trajectories of each simulation algorithm to produce the results.

Table S17: Species in the Cell Cycle network and their initial concentrations.

	Name	Description	Initial values ODE solution 1 Fig. S20	Initial values ODE solution 2 Fig. S20
1	x_1	Cdc2-Cyclin B	0.9300	0.8400
2	y_1	Wee1	0.9100	0.9900

Table S18: Parameters used in the Cell Cycle network.

Parameter	Description	Value	Unit
a_1	Production rate of x_1	1	s^{-1}
a_2	Production rate of y_1	1	s^{-1}
b_1	Hill coefficient for y_1 regulation of x_1	200	–
b_2	Hill coefficient for x_1 regulation of y_1	10	–
γ_1	Hill exponent for y_1 regulation of x_1	4	–
γ_2	Hill exponent for x_1 regulation of y_1	4	–
K_1	Half-activation constant for x_1 regulation of y_1	2.3403	–
K_2	Half-activation constant for y_1 regulation of x_1	1	–
A	External activation strength	1	–

Table S19: The RRE ODEs for the mean-field dynamics of the Cell Cycle system in the limit $\Omega \rightarrow \infty$.

$$\begin{aligned} \dot{x}_1 &= a_1 - a_1 x_1 - \frac{b_1 x_1 ((A y_1)^{\gamma_1})}{K_1^{\gamma_1} + (A y_1)^{\gamma_1}} \\ \dot{y}_1 &= a_2 - a_2 y_1 - \frac{b_2 y_1 (x_1^{\gamma_2})}{K_2^{\gamma_2} + x_1^{\gamma_2}} \end{aligned}$$

Table S20: Reactions and their corresponding propensity functions for SSA simulations.

Reaction	Propensity function
$X_1 \xrightarrow{a_1} X_1$	$\pi_1 = a_1 \cdot \Omega$
$X_1 \rightarrow \emptyset$	$\pi_2 = Y_1$
$X_2 \xrightarrow{b_1} X_2$	$\pi_3 = \frac{b_1 Y_1 ((A Y_2)^{\gamma_1})}{(K_1 \Omega)^{\gamma_1} + (A Y_2)^{\gamma_1}}$
$X_2 \rightarrow \emptyset$	$\pi_4 = Y_2$
$Y_1 \xrightarrow{a_2} Y_1$	$\pi_5 = a_2 \cdot \Omega$
$Y_1 \rightarrow \emptyset$	$\pi_6 = Y_2$
$Y_2 \xrightarrow{b_2} Y_2$	$\pi_7 = \frac{b_2 Y_2 ((Y_1)^{\gamma_2})}{(K_2 \Omega)^{\gamma_2} + (Y_1)^{\gamma_2}}$
$Y_2 \rightarrow \emptyset$	$\pi_8 = Y_3$

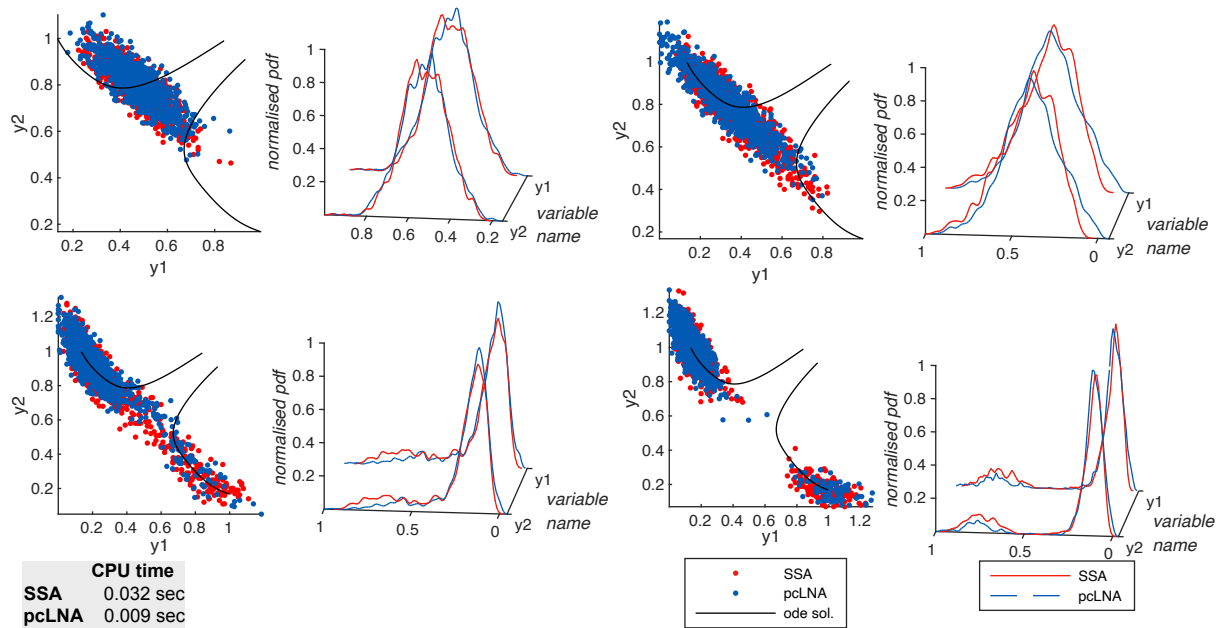


Figure S20: Comparison between SSA (red) and pcLNA (blue) for the Cell Cycle network at $\Omega = 100$. Panels (A)–(D) correspond to times $t = 0.5000, 9.9999, 49.9996, 100.0000$, respectively. Each panel shows (left) the states recorded at time t of the simulations with solutions of the corresponding RRE, and (right) the corresponding empirical probability density functions of each system variable. The initial conditions for the two ODE solutions are provided in Table S17, and the parameter values are given in Table S18.

S4.6 The Somitogenesis Switch reaction network

The system is described in [19]. The tables S21, S22, S23, S24 describe the species and their initial conditions, the parameters, the ODE system, and the propensity functions of the SSA simulations of this system, respectively. The results in Figure S21 are derived using the same method as used for Figure 3 in the main paper. The computation of the empirical density functions is done as described in SI section S4.1.1. We used 1000 trajectories of each simulation algorithm to produce the results.

Table S21: Species in the Somitogenesis Switch network and their initial concentrations.

	Name	Description	Initial values ODE solution 1 Fig. S21	Initial values ODE solution 2 Fig. S21
1	R	Retinoic Acid (RA)	1.1500	1.2000
2	M_C	cyp26 mRNA	1.7467	1.7067
3	C	CYP26 protein	6.2333	6.0900
4	F	FGF8 protein	0.4933	0.4800

Table S22: Parameters used in the Somitogenesis Switch network.

Parameter	Description	Value	Unit
k_{s1}	RA synthesis rate via RALDH2	1	s^{-1}
RALDH2	RA synthetase concentration	7.1	–
k_{d1}	RA degradation via CYP26	1	s^{-1}
k_{d5}	Basal RA degradation	0	s^{-1}
V_0	Basal transcription of M_C	0.365	s^{-1}
V_{sc}	Activated transcription of M_C	7.1	s^{-1}
K_a	Activation constant for M_C production	0.5	–
n	Hill coefficient for FGF activation of M_C	2	–
k_{d3}	mRNA degradation rate	1	s^{-1}
k_{s2}	Translation rate of CYP26	1	s^{-1}
k_{d2}	CYP26 degradation rate	0.28	s^{-1}
k_{s3}	FGF8 synthesis rate	1	s^{-1}
M_0	Baseline activator level for FGF synthesis	5	–
K_I	Inhibition constant for RA effect on FGF	0.5	–
m	Hill coefficient for RA inhibition of FGF	2	–
k_{d4}	FGF degradation rate	1	s^{-1}
L	Normalization constant for spatial scaling	50	–
A	External activation strength	1	–

Table S23: The RRE ODEs for the mean-field dynamics of the Somitogenesis Switch in the limit $\Omega \rightarrow \infty$.

$$\begin{aligned}
\dot{R} &= k_{s1} \cdot \text{RALDH2} - k_{d1}RC - k_{d5}R \\
\dot{M}_C &= V_0 + \frac{V_{sc}F^n}{K_a^n + F^n} - k_{d3}M_C \\
\dot{C} &= k_{s2}M_C - k_{d2}C \\
\dot{F} &= k_{s3} \cdot \frac{M_0A/L \cdot K_I^m}{K_I^m + R^m} - k_{d4}F
\end{aligned}$$

Table S24: Reactions and their corresponding propensity functions for SSA simulations.

Reaction	Propensity function
$R \xrightarrow{\text{syn}} R$	$\pi_1 = \Omega \cdot k_{s1} \cdot \text{RALDH2}$
$R + C \xrightarrow{\text{deg}} \emptyset$	$\pi_2 = \frac{k_{d1}RC}{\Omega}$
$R \xrightarrow{\text{deg}} \emptyset$	$\pi_3 = k_{d5}R$
$M_C \xrightarrow{\text{basal}} M_C$	$\pi_4 = \Omega \cdot V_0$
$M_C \xrightarrow{\text{FGF act}} M_C$	$\pi_5 = \frac{\Omega \cdot V_{sc} F^n}{(\Omega K_a)^n + F^n}$
$M_C \xrightarrow{\text{deg}} \emptyset$	$\pi_6 = k_{d3}M_C$
$C \xrightarrow{\text{trans}} C$	$\pi_7 = k_{s2}M_C$
$C \xrightarrow{\text{deg}} \emptyset$	$\pi_8 = k_{d2}C$
$F \xrightarrow{\text{syn}} F$	$\pi_9 = \frac{\Omega \cdot k_{s3} \cdot (M_0A/L) \cdot (\Omega K_I)^m}{(\Omega K_I)^m + R^m}$
$F \xrightarrow{\text{deg}} \emptyset$	$\pi_{10} = k_{d4}F$

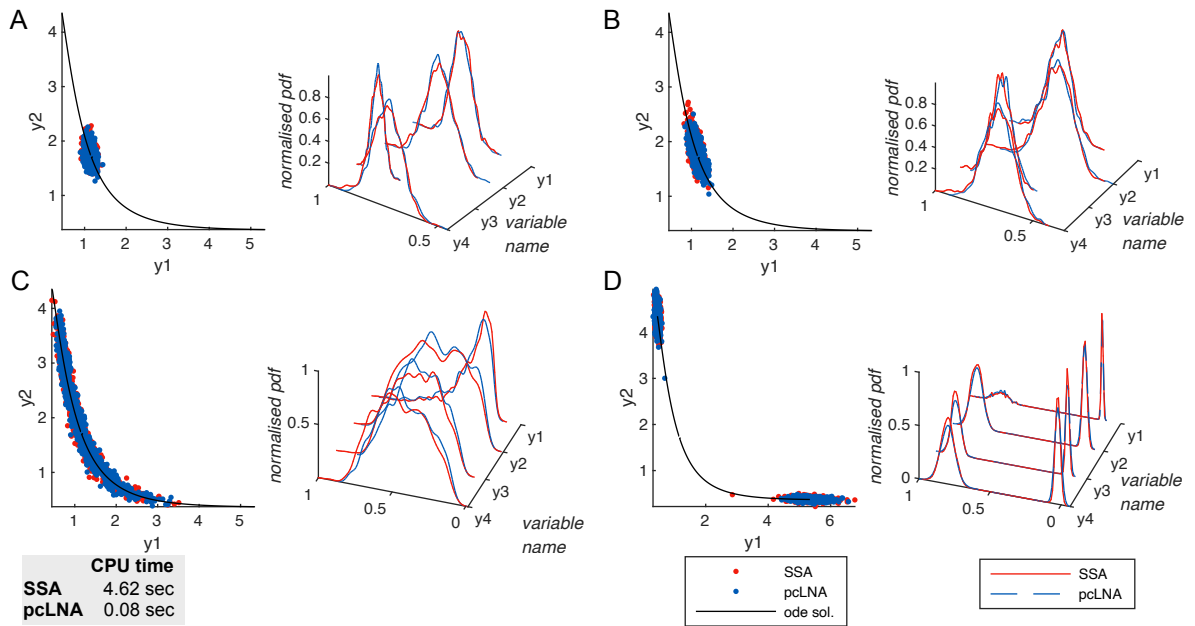


Figure S21: Comparison between SSA (red) and pcLNA (blue) for the Somitogenesis Switch network at $\Omega = 300$. Panels (A)–(D) correspond to times $t = 2, 5, 20, 99$, respectively. Each panel shows (left) the states recorded at time t of the simulations with solutions of the corresponding RRE, and (right) the corresponding empirical probability density functions of each system variable. The initial conditions for the two ODE solutions are provided in Table S21, and the parameter values are given in Table S22.